

# Contents

<b>1. Introduction</b>	<b>1</b>
<b>2. Physics of the VIP2 experiment</b>	<b>3</b>
2.1. Physics Basics . . . . .	3
2.1.1. The Pauli Exclusion Principle . . . . .	3
2.1.2. Quantum Mechanical Angular Momenta . . . . .	4
2.1.3. The Spin . . . . .	6
2.1.4. Indistinguishability, Symmetrization Postulate and Supers-election Rule . . . . .	8
2.1.5. Fermions, Bosons and the Spin-Statistics Connection . . . . .	11
2.2. Theories of Violation of Spin-Statistics . . . . .	13
2.2.1. Parastatistics . . . . .	14
2.2.2. The Ignatiev and Kuzmin Model and Parons . . . . .	14
2.2.3. Quons . . . . .	15
2.3. Tests of the Pauli Exclusion Principle . . . . .	16
2.3.1. Remarks on testing the Pauli Exclusion Principle . . . . .	16
2.3.2. Experiments for testing the Pauli Exclusion Principle . . . . .	17
2.4. The VIP2 experimental method . . . . .	20
<b>3. The Measurement Setup</b>	<b>25</b>
3.1. Silicon Drift Detectors and copper target . . . . .	25
3.1.1. Working principle . . . . .	26
3.1.2. SDD specifications for the VIP2 experiment . . . . .	27
3.1.3. Silicon Drift Detectors performance characteristics . . . . .	29
3.2. Active Shielding . . . . .	30
3.2.1. Scintillators . . . . .	31
3.2.2. Silicon Photomultipliers . . . . .	32
3.3. Cooling system . . . . .	32
3.4. Data acquisition and slow control systems . . . . .	34
3.4.1. Signal readout and data acquisition . . . . .	34
3.4.2. Slow control . . . . .	36

<b>4. Simulations</b>	<b>39</b>
4.1. Detection Efficiency . . . . .	39
4.2. Cosmic Ray Background . . . . .	41
4.3. Gamma Ray Background . . . . .	44
<b>5. Test Measurements</b>	<b>47</b>
5.1. Test Measurements at LNF . . . . .	47
5.2. Test Measurements at SMI . . . . .	48
5.2.1. Water Cooling of Cu Target . . . . .	49
5.2.2. Argon Cooling of Silicon Drift Detectors . . . . .	50
5.2.3. Scintillator Energy Deposition Trigger Threshold . . . . .	51
5.2.4. SDD Energy Resolution . . . . .	52
5.2.5. SDD Time Resolution . . . . .	54
5.2.6. Scintillator plus SiPM Time Resolution . . . . .	54
5.2.7. Detection Efficiency of Cosmic Radiation and Active Shielding Test . . . . .	56
<b>6. Data Taking at LNGS and Data Analysis</b>	<b>63</b>
6.1. Comparison of Data and Simulations . . . . .	65
6.2. Effects of 100 A Current . . . . .	67
6.3. Spectral Lines in the Energy Spectrum . . . . .	69
6.4. Data Selection . . . . .	70
6.5. Energy Calibration . . . . .	72
6.6. Peak Stability and Data Splitting . . . . .	75
6.7. Scale Linearity and 2 <sup>nd</sup> Order Scale Correction . . . . .	77
<b>7. Conclusion</b>	<b>83</b>
<b>Bibliography</b>	<b>i</b>
<b>Appendices</b>	<b>ix</b>
<b>A. Data Acquisition Layout</b>	<b>xi</b>

# 1. Introduction

The Pauli Exclusion Principle (PEP) is a fundamental principle in physics, valid for identical-fermion systems. It was formulated in 1925 by the austrian physicist Wolfgang Pauli. It states that two fermions (particles with half integer spin) can not occupy the same quantum state simultaneously. Examples for fermionic particles are elementry particles such as quarks, leptons (electron, muon and tauon) and neutrinos. Also composite particles can be fermions (e.g. protons and neutrons). Electrons, which make up the electronic shell of atoms, are fermions and therefore obey the PEP. For the case of electronic shells the PEP is equivalent to the statement that two electrons can not have the same principal quantum number  $n$ , angular momentum quantum number  $l$ , magnetic quantum number  $m_l$  and spin quantum number  $m_s$  at the same time. This means that two electrons can share the quantum numbers  $n$ ,  $l$  and  $m_l$ , as long as they have different spin quantum number  $m_s$  ( $\pm \frac{1}{2}$ ).

The PEP forms the basis of the periodic table of elements, as it prevents all electrons in a shell to condense into the ground state. Therefore it is responsible for the occupation of the electronic shells and the chemical properties of elements. Also it is connected to the stability of neutron stars, as the neutron degeneracy pressure, which is caused by the PEP, prevents them from collapsing under their own gravitational pressure. Another phenomenon it is intimately connected to is electric conductivity, which will be described in chapter 2.

Due to the fundamental place of the PEP in quantum field theory, many researches were interested in testing it. In the year 1948, the Pauli Exclusion Principle was tested by Goldhaber and Scharff-Goldhaber [1]. Their experiment was designed to determine if the particles making up  $\beta$ -radiation were the same as electrons, but it was later used to test the Pauli Exclusion Principle. The experiment was done by shining electrons the particles from a  $\beta$  source onto a block of lead. The authors thought, if these  $\beta$  particles were different from electrons, they could be captured by the lead atoms and cascade down to the ground state without being subject to the PEP. The X-rays emitted during this cascading process were used to set an upper bound for the probability that the PEP is violated. Another

thorough test was conducted in 1988 by E. Ramberg and G. A. Snow [2]. They introduced a current into a copper conductor. The electrons of the current then had a chance to be absorbed by the copper atoms and form a new quantum state. The experimenters searched for states having a symmetric component in an otherwise antisymmetric state. These states were identified by X-rays they emitted while cascading to the ground state. The same principle was later employed in the VIP experiment, which was able to set a new upper limit for the probability for the violation of the Pauli Exclusion Principle of:

$$\frac{\beta^2}{2} \leq 4.7 * 10^{-29}$$

([3], [4]). The follow-up experiment VIP2 is currently taking data in the Laboratori Nazionali del Gran Sasso (LNGS). The current results, the setup configuration and various other aspects of this experiment will be discussed in the following chapters.

## 2. Physics of the VIP2 experiment

discovery of the pep?; spin, pep and the spin statistics connection - 2nd quantization - symm/antisymm wfkt; exchange interaction; symmetrization postulate??; group theory + young diagrams; theories of violation of spin Statistics, mg supers-election rule, electrons in a conductor - formation of electric current - decoherence of electrons ? - interaction of an electron with an atom - cascading process; current on/off -> vip2 mesurement principle; and why it is better than other experiments (steady state interactions)

### 2.1. Physics Basics

#### 2.1.1. The Pauli Exclusion Principle

To explain the spectra of alkali atoms, recorded with a magnetic field (Zeemann effect), Wolfgang Pauli postulated a 4<sup>th</sup> quantum number for electrons in the early 1920s. This one was in addition to the quantum numbers already known to that time, which are nowadays called principal quantum number  $n$ , angular momentum quantum number  $l$  and magnetic quantum number  $m_l$ . He named this quantum number a “two-valuedness not describable classically” [5]. This 4<sup>th</sup> quantum number was later called the electron’s spin. Another problem he was working on at that time was the series of integer number 2, 8, 18, 32, etc., which was determining the lengths of the lines in what we call the periodic table of elements. It was furthermore known to him that the number of electronic energy levels in an alkali atom were the same as the number of electrons in the closed shell of the rare gas with the same principal quantum number. He used this information to formulate the Pauli Exclusion Principle: The number of electrons in closed subgroups can be reduced to one, if the division of the groups (by giving them values of the four quantum numbers) is carried so far that every degeneracy

is removed. An entirely non-degenerate level is closed, if it is occupied by a single electron [5]. This is equivalent to saying that every state corresponding to a set of quantum numbers  $n$ ,  $l$ ,  $m_l$  and  $m_s$  can only be occupied by one electron. Wolfgang Pauli won the Nobel Prize in physics for the formulation of the Pauli Exclusion principle in 1945. It was first formulated for electrons, but later on extended to all fermions.

### 2.1.2. Quantum Mechanical Angular Momenta

angular momentum + magnetic moment -classically;  $l_z$ ,  $l_2$  operator,eigenvalues, degeneracy; commutation relations -> also with hamiltonian -> conservation

From a classical point of view an angular momentum is defined as:  $\vec{L} = \vec{r} \times \vec{p}$ . In this formula  $\vec{L}$  is the angular momentum,  $\vec{r}$  is the vector to the particle from the origin and  $\vec{p}$  is the momentum of the particle. The magnetic moment of a particle with charge  $q$  moving in a circle with radius  $r$  is defined as  $\vec{\mu} = I \times \vec{A}$ . Here  $\vec{\mu}$  is the magnetic moment,  $\vec{A} = r^2\pi * e_A$  is the area that the particle's movement is encircling and  $I$  is the current. The current the particle generates can be written as:

$$I = \frac{q}{T} = \frac{q}{\frac{2r\pi}{v}} = \frac{qv}{2r\pi} \quad (2.1)$$

Here,  $v$  is the particle's velocity and  $T$  is the time it needs for one full circle. After dropping the vector arrows due to orthogonality, the magnetic moment can be written as:

$$\mu = IA = \frac{qv}{2r\pi} r^2\pi = \frac{qvr}{2} = \frac{q}{2m} rvm = \frac{q}{2m} L \quad (2.2)$$

Where  $\frac{q}{2m} = \frac{\mu}{L}$  is called the gyromagnetic ratio. Formula 2.2 is for electrons often rewritten in the form

$$\mu_e = g\mu_B \frac{L}{\hbar} \quad \mu_B = \frac{e\hbar}{2m_e} \quad \hbar = 1.054571800(13) \times 10^{-34} \left[ \frac{m^2 kg}{rad \times s} \right] \quad (2.3)$$

where  $\mu_e$  is the magnetic moment of the electron,  $m_e$  is the electron mass and  $\mu_B$  is the Bohr magneton. The Bohr magneton is the expected ratio between the magnetic moment  $\mu_e$  and the dimensionless value  $\frac{L}{\hbar}$ . The *g-factor* parametrizes deviations from the expected value  $g = 1$ , which could arise, if for example the charge density distribution is different from the mass density distribution.

In analogy to classical mechanics, the angular momentum can be written in quantum mechanics as a cross product of the position operator  $\hat{x}$  and the momentum

operator  $\hat{p}$ :  $\hat{L} = \hat{x} \times \hat{p}$ . In position basis this can be written as

$$\hat{L} = \hat{x} \times \hat{p} = \frac{\hbar}{i}(\vec{x} \times \vec{\nabla}) \quad \vec{\nabla} = \begin{pmatrix} \frac{\partial}{\partial x} \\ \frac{\partial}{\partial y} \\ \frac{\partial}{\partial z} \end{pmatrix} \quad (2.4)$$

In index notation, this operator can also be written as follows:  $\hat{L}_i = \epsilon_{ijk}x_j\hat{p}_k$  with  $\epsilon_{ijk}$  being the antisymmetric Levi-Civita tensor. The indices  $i, j, k$  correspond to the 3 spatial dimensions.  $\hat{L}_i$  and  $\hat{L}_j$  do not commute as

$$[\hat{L}_i, \hat{L}_j] = i\hbar\epsilon_{ijk}\hat{L}_k \quad [\hat{X}, \hat{Y}] = \hat{X}\hat{Y} - \hat{Y}\hat{X} \quad (2.5)$$

Here  $[\hat{X}, \hat{Y}]$  denotes the commutator of  $\hat{X}$  and  $\hat{Y}$ . For readability, the hats of operators will be omitted from now on. The entries  $L_i$  of the angular momentum operator commute with the rotation invariant form  $L^2 = L_x^2 + L_y^2 + L_z^2$ . This is the operator of the squared norm of the angular momentum.  $L_i$  and  $L^2$  are compatible variables and can be measured simultaneously. This also means that

$$[L_i, L^2] = 0 \quad (2.6)$$

For any given system, the following relations for the eigenvalues of these operators hold:

$$L_i |\phi\rangle = m_l \hbar |\phi\rangle \quad m_l \in \dots - 2, -1, 0, 1, 2, \dots \quad (2.7)$$

$$L^2 |\phi\rangle = \hbar^2 l(l+1) |\phi\rangle \quad l \in 0, 1, 2, \dots \quad (2.8)$$

with  $|m_l| \leq l$ . Considering now particles without spin and and rotation symmetric Hamiltonian of the form  $H = \frac{p^2}{2m} + V(r)$  (like the atom), the angular momentum is conserved and commutes with the Hamiltonian

$$[H, L_i] = [H, L^2] = [L_i, L^2] = 0 \quad (2.9)$$

Therefore  $L_i$  and  $L^2$  are conserved quantities. For systems without spin,  $H$ ,  $L^2$  and  $L_i$  form a complete set of commuting observables with the corresponding quantum numbers  $n$  (principal quantum number),  $l$  (angular momentum quantum number) and  $m_l$  (magnetic quantum number). Introducing the rotation invariant Coulomb potential for  $V(r)$

$$V(r) = -\frac{1}{4\pi\epsilon_0} \frac{q}{r} \quad (2.10)$$

one finds that angular momentum quantum number  $l$  always needs to be smaller than the principal quantum number  $n$  ( $l < n$ ). Only considering pure Coulomb interaction, the eigenstates with principal quantum number  $n$  belonging to the eigenvalue  $E_n$  are  $n^2$ -fold degenerate.

### 2.1.3. The Spin

orbital angular mom + spin: 2 diff types , spin angular momenta can take half integer values; spin has magnitude: all particles of same type- same, kg m<sup>2</sup>s<sup>-1</sup>, dimensionless spin quantum number, spin can not be made higher or lower (contrast to ang mom), algabra and formulas; J=L+S commutation with H; pauli matrices

The spin is an intrinsic form of angular momentum carried by elementary particles. It has a definitive and non-modifiable magnitude for each particle type. This is a difference to the section 2.1.2, where the angular momenta, described by the quantum number  $l$ , could change in magnitude. Wolfgang Pauli was the first to propose the concept of spin in 1925. Analogous to the relation between angular momentum and magnetic moment 2.3, the relation between spin and angular momentum can be written as

$$\mu_s = g\mu_B \frac{S}{\hbar} \quad \mu_B = \frac{e\hbar}{2m} \quad (2.11)$$

where  $\mu_s$  is the magnetic moment of a particle due to its spin and  $S$  is the magnitude of this spin. Unlike for angular momenta described in 2.1.2, the value for  $g \neq 1$ . From the Dirac equation, a value of  $g = 2$  can be obtained. Corrections for example from Quantum Electrodynamics further alter this value on the %-level.

Analogous to equation 2.5 and 2.6, commutation relations can be found for the spin:

$$[S_i, S_j] = i\hbar\epsilon_{ijk}S_k \quad (2.12)$$

$$[S_i, S^2] = 0 \quad (2.13)$$

Here  $S_i$  are the spin components in one spatial direction and  $S^2$  is the squared norm of the spin. Furthermore, analogous to equations 2.7 and 2.8 following relations hold for the spin:

$$S^2 |\phi\rangle = \hbar^2 s(s+1) |\phi\rangle \quad s \in 0, \frac{1}{2}, 1, \dots \quad (2.14)$$

$$S_i |\phi\rangle = m_s \hbar |\phi\rangle \quad |m_s| \leq s \quad (2.15)$$

Here  $s$  is the spin quantum number and  $m_s$  is the spin projection quantum number. The big difference between  $s$  and its analogon  $l$  from the previous chapter is that  $s$  can also take half-integer values. Another difference is, that  $s$ , unlike  $l$  can not be changed and is intrinsic for each particle type. Particles with half-integer spin quantum number are called *fermions*, particles with integer spin are called *bosons*.

In particular, leptons such as electrons have  $s = \frac{1}{2}$  and therefore  $m_s$  can take the values  $\pm \frac{1}{2}$ . For a system containing particles with spin,  $n$ ,  $l$ ,  $m_l$  and  $m_s$  form a complete set of commuting observables. The total angular momentum ( $\vec{J}$ ) can be defined as the sum of the orbital angular momentum and spin  $\vec{J} = \vec{L} + \vec{S}$ . Analogous expressions to equations 2.5 - 2.9 hold for the total angular momentum  $\vec{J}$  in systems containing particles with spin.

Considering a system containing a particle with  $s = \frac{1}{2}$ . The basis in which  $S^2$  and  $S_z$  are diagonal consists of two states  $|s, m_s\rangle = |\frac{1}{2}, \pm \frac{1}{2}\rangle$ . These states can be identified with the basis vectors  $e_1 = \begin{pmatrix} 1 \\ 0 \end{pmatrix}$  and  $e_2 = \begin{pmatrix} 0 \\ 1 \end{pmatrix}$  and are often referred to as “spin-up” and “spin-down” relative to a defined z-direction. The action of operators on these states is as follows:

$$S^2 \left| \frac{1}{2}, \pm \frac{1}{2} \right\rangle = \hbar^2 \frac{1}{2} \left( \frac{1}{2} + 1 \right) \left| \frac{1}{2}, \pm \frac{1}{2} \right\rangle \quad (2.16)$$

$$S_z \left| \frac{1}{2}, \frac{1}{2} \right\rangle = \hbar \frac{1}{2} \left| \frac{1}{2}, \frac{1}{2} \right\rangle \quad (2.17)$$

$$S_z \left| \frac{1}{2}, -\frac{1}{2} \right\rangle = -\hbar \frac{1}{2} \left| \frac{1}{2}, -\frac{1}{2} \right\rangle \quad (2.18)$$

$$S_+ \left| \frac{1}{2}, \frac{1}{2} \right\rangle = 0 \quad S_- \left| \frac{1}{2}, \frac{1}{2} \right\rangle = \hbar \left| \frac{1}{2}, -\frac{1}{2} \right\rangle \quad (2.19)$$

$$S_+ \left| \frac{1}{2}, -\frac{1}{2} \right\rangle = \hbar \left| \frac{1}{2}, \frac{1}{2} \right\rangle \quad S_- \left| \frac{1}{2}, -\frac{1}{2} \right\rangle = 0 \quad (2.20)$$

The *ladder operators* ( $S_{\pm}$ ) were used in equations 2.19 and 2.20. A ladder operator increases ( $S_+$ ) or decreases ( $S_-$ ) the azimuthal quantum number of a state and for an angular momentum  $\vec{J}$  with quantum numbers  $j$  and  $m_j$  defined as

$$J_{\pm} |j, m_j\rangle = \hbar \sqrt{(j \mp m_j)(j \pm m_j + 1)} |j, m_j \pm 1\rangle \quad (2.21)$$

In the mentioned basis, the operators  $S_x$ ,  $S_y$  and  $S_z$  can be written as

$$S_x = \frac{\hbar}{2} \begin{pmatrix} 0 & 1 \\ 1 & 0 \end{pmatrix}, \quad S_y = \frac{\hbar}{2} \begin{pmatrix} 0 & -i \\ i & 0 \end{pmatrix}, \quad S_z = \frac{\hbar}{2} \begin{pmatrix} 1 & 0 \\ 0 & -1 \end{pmatrix} \quad (2.22)$$

These are the so called *Pauli matrices*.

## 2.1.4. Indistinguishability, Symmetrization Postulate and Superselection Rule

indistinguishability of identical particles  $\rightarrow [P, A] = [P, H] = 0$  invariance of observables under permutations \*  $\rightarrow$  invariance of the hamiltonian  $\rightarrow$  possible wfkt  $\rightarrow$  symmetrization postulate (arguments against)  $\rightarrow$  division into fermions and bosons  $\rightarrow$  simple argument for PEP; bosonic and fermionic statistics (occupation number)

The following section loosely based on [6]. First, let us define the action of the permutation operator  $P_{i,j}$  on a given state  $\phi = \phi(1, 2, \dots, i, \dots, j, \dots, N)$ , where the variables 1, 2, ... denote the spatial and the spin degrees of freedom. The permutation operator is defined as

$$P_{i,j} \phi(1, 2, \dots, i, \dots, j, \dots, N) = \phi(1, 2, \dots, j, \dots, i, \dots, N) \quad (2.23)$$

The indistinguishability of identical particles implies that states that differ only by a permutation of identical particles can not be distinguished by any measurement. In quantum mechanics, a measurement is expressed as the expectation value of a hermitian <sup>1</sup> operator  $A$ . This statement can be expressed for a state  $\phi$  as the following equation:

$$\langle \phi | A | \phi \rangle = \langle \phi | P^\dagger A P | \phi \rangle \quad (2.24)$$

From this equation follows that the permutation operator commutes with every observable, as it holds for every state  $\phi$  and it follows that  $P^\dagger A P = A$ . Therefore  $PA = AP$  which implies commutation of the 2 operators. Specifically, the energy of a quantum mechanical system also must not depend on the permutation of identical particles. From above considerations it follows that:

$$[P, H] = 0 \quad (2.25)$$

where  $H$  is the Hamiltonian.

An infinitesimal time evolution of a state is given by the Schrödinger equation

$$\partial_t |\phi(t)\rangle = \frac{1}{i\hbar} H |\phi(t)\rangle \Rightarrow |\phi(t + \delta t)\rangle = (1 + \frac{\delta t}{i\hbar} H + O(\delta t^2)) |\phi(t)\rangle \quad (2.26)$$

For a time-independent Hamiltonian  $H$ ,  $n \rightarrow \infty$  infinitesimal time steps between a start time  $t_0$  and time  $t$  give the time evolution operator  $U(t - t_0)$ :

$$|\phi(t)\rangle = U(t - t_0) |\phi(t_0)\rangle \quad U(t - t_0) = e^{-\frac{i}{\hbar}(t-t_0)H} \quad (2.27)$$

---

<sup>1</sup>A hermitian or self-adjoint operator is an operator for which the relation  $A^\dagger = A$  holds. The hermitian conjugation  $^\dagger$  corresponds to transposition combined with complex conjugation. A hermitian operator has real eigenvalues and eigenvectors for different eigenvalues are orthogonal.

As the permutation operator commutes with the Hamiltonian, it also commutes with the time evolution operator  $U$ ,

$$[P, U] = 0 \quad (2.28)$$

because of equation 2.27. Therefore, the permutation symmetry of a state is conserved. This is called the *Messiah-Greenberg (MG) superselection rule*. It is important to note that above considerations are only viable for systems where the number of particles is conserved and that the symmetry of a system is not necessarily preserved in systems with a non-constant particle number (see for example [7]).

Let us consider now a system of 2 particles. The state  $|\phi(1, 2)\rangle$  is a solution of the Schrödinger equation

$$H |\phi(1, 2)\rangle = E |\phi(1, 2)\rangle \quad (2.29)$$

As the Hamiltonian commutes with the permutation operator,  $P_{12} |\phi(1, 2)\rangle = |\phi(2, 1)\rangle$  is also a solution to this equation with the same Hamiltonian  $H$  and the same eigenvalue  $E$ . All linear combinations of these 2 functions are also solutions of the equation. The linear combinations  $|\Phi\rangle = |\phi(1, 2)\rangle \pm |\phi(2, 1)\rangle$  represent solutions corresponding to positive and negative symmetry with respect to particle exchange.

The situation is a bit more complex for a system with 3 particles. In case the state  $|\phi(1, 2, 3)\rangle$  solves the Schrödinger equation, the linear combination:

$$|\phi(1, 2, 3)\rangle + |\phi(1, 3, 2)\rangle - |\phi(3, 2, 1)\rangle \quad (2.30)$$

also solves the Schrödinger equation. For an exchange of particles 1 and 2, this state becomes

$$|\phi(2, 1, 3)\rangle + |\phi(2, 3, 1)\rangle - |\phi(3, 1, 2)\rangle \quad (2.31)$$

The state is not an eigenstate of the permutation operator  $P_{12}$ . Therefore not all solutions of the Schrödinger equation need to be eigenfunctions of the permutation operator. A special case are the linear combinations with negative:

$$|\phi(1, 2, 3)\rangle - |\phi(1, 3, 2)\rangle - |\phi(2, 1, 3)\rangle + |\phi(2, 3, 1)\rangle + |\phi(3, 1, 2)\rangle - |\phi(3, 2, 1)\rangle \quad (2.32)$$

and positive:

$$|\phi(1, 2, 3)\rangle + |\phi(1, 3, 2)\rangle + |\phi(2, 1, 3)\rangle + |\phi(2, 3, 1)\rangle + |\phi(3, 1, 2)\rangle + |\phi(3, 2, 1)\rangle \quad (2.33)$$

symmetry with respect to particle exchange. These linear combinations are called completely (anti-)symmetric. This means that an application of the permutation

operator for any pair of particles gives a negative or positive sign for the state  $P|\Phi\rangle = \pm|\Phi\rangle$ .

For a general system of  $N$  particles, the symmetry of different linear combinations of wave functions are described by *Young diagrams* (see for example [8]). A Young diagram represents an irreducible representation of the permutation group <sup>2</sup>. An example for such diagrams is shown in figure 2.1 Each box of a Young diagram

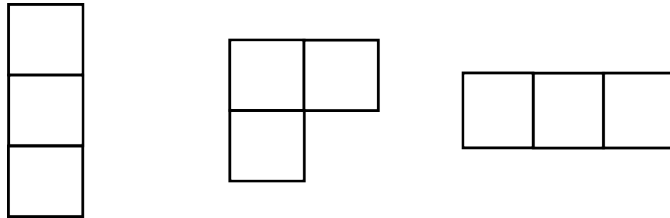


Figure 2.1.: Young diagrams of the  $S_3$  permutation group for antisymmetric (left), mixed (middle) and symmetric (right) permutation symmetry.

symbolizes a particle and the spatial relation of 2 boxes symbolizes the permutation symmetry of the state with respect to exchange of the particles in the boxes. 2 boxes arranged vertically stand for antisymmetric exchange symmetry and 2 boxes aligned horizontally mean symmetric exchange symmetry. From the description of this kind follows that all states described by a Young diagram are eigenstates of the permutation operator. In figure 2.1 different exchange symmetries for systems with 3 particles are shown. It is important to note that there is not only the completely (anti-)symmetric exchange symmetry (left/right side), but also the state with a positive symmetry for the exchange of one pair of particles and negative symmetry for another pair. This state is called a mixed-symmetry state.

The *symmetrization postulate* states that from the 3 different permutation symmetries in figure 2.1, only the left and the right ones are realised in nature [7]. Due to their form they are called the one-dimensional representation of the permutation group. The usual proof of this postulate is like this:

The indistinguishability of identical particles results in the fact that a permutation of 2 particles should only multiply the wave function only by an insignificant phase factor  $e^{i\alpha}$  with  $\alpha$  being a real constant.

$$P_{12}|\phi(1, 2)\rangle = |\phi(2, 1)\rangle = e^{i\alpha}|\phi(1, 2)\rangle \quad (2.34)$$

---

<sup>2</sup>The permutation group  $S_N$  is a group whose elements are the permutations of a set with  $N$  elements.

One more application of the permutation operator gives

$$P_{12}P_{12} |\phi(1, 2)\rangle = |\phi(1, 2)\rangle = e^{i\alpha}e^{i\alpha} |\phi(1, 2)\rangle = e^{2i\alpha} |\phi(1, 2)\rangle \quad (2.35)$$

or

$$e^{2i\alpha} = 1 \Rightarrow e^{i\alpha} = \pm 1 \quad (2.36)$$

As it is shown in [8], this proof is incorrect. One argument against this proof is that the indistinguishability of identical particles only requires the squared norm of the wave function to be invariant under permutations:

$$P_{12} | |\phi(1, 2)\rangle |^2 = | |\phi(1, 2)\rangle |^2 \quad (2.37)$$

For a function to satisfy this relation it is sufficient that it changes under permutations as:

$$P_{12} |\phi(1, 2)\rangle = e^{i\alpha(1,2)} |\phi(1, 2)\rangle \quad (2.38)$$

where 1 and 2 are as in the above formulas the space and the spin coordinates of the two particles. So in general the phase factor can be a function of the permutation and of the coordinates. That means that in general, equations 2.35 and 2.36 do not hold. Consequently the symmetrization postulate states the fact that only the one-dimensional representations of the permutation group meaning the fully (anti-) symmetric states have yet been observed in nature and the solution of the Schrödinger equation can belong to any representation of the permutation group, not only the one-dimensional ones.

### 2.1.5. Fermions, Bosons and the Spin-Statistics Connection

As mentioned in section 2.1.3, different particles have different intrinsic spin, which can not be altered. As was shown in 1940 by Wolfgang Pauli [9], the spin of a particle determines which of the 2 possible representations of the permutation group it belongs to.

Particles with integer spin ( $s = 0, 1, 2, \dots$ ) have symmetric wave functions with respect to particle exchange. These particles are called *bosons* (after Indian physicist Satyendra Nath Bose). Their corresponding Young diagram is of the type on the right side of figure 2.1. Elementary bosonic particles are for example the force carrier particles of strong, weak and electromagnetic interaction: the gluon, the W and Z bosons and the photon. Another example for an elementary boson is the Higgs particle. Composite bosons can be made up out of particles with half integer or with integer spin. Examples for this kind of particles are mesons, which are made up out of 2 quarks with  $s = \frac{1}{2}$ .

The occupation number of bosons follows the Bose-Einstein statistics. The expected number of particles in an energy state is in this case:

$$N(E) = \frac{1}{e^{\frac{E-\mu}{kT}} - 1} \quad (2.39)$$

where  $E$  is the energy of the state,  $\mu$  is the chemical potential,  $k$  is the Boltzmann constant and  $T$  is the absolute temperature. A consequence of this statistics is that more than one bosonic particles can occupy the same quantum state. The commutation relations of creation ( $a^\dagger$ ) and annihilation ( $a$ ) operators for bosonic particles in states  $X$  and  $Y$  are:

$$[a_X, a_Y] = 0 \quad [a_X^\dagger, a_Y^\dagger] = 0 \quad [a_X, a_Y^\dagger] = \delta_{X,Y} \quad (2.40)$$

Particles with half-integer spin ( $s = \frac{1}{2}, \frac{3}{2}, \dots$ ) have antisymmetric wave functions with respect to particle exchange. This means changing the position of 2 particles multiplies the wave function with a minus sign. These particles are called *fermions* (after the Italian physicist Enrico Fermi). Their corresponding Young diagram is of the type on the left side of figure 2.1. Fermions can be elementary particles like quarks, electrons, neutrons or positrons, but also composite particles like atoms.

The occupation number of fermions follows the Fermi-Dirac statistics. The expected number of particles in an energy state is in this case:

$$N(E) = \frac{1}{e^{\frac{E-\mu}{kT}} + 1} \quad (2.41)$$

As the exponential function is always positive, the occupation number is always smaller than 1. This means that every energy state can only be occupied by 1 fermion. This is known as the *Pauli Exclusion Principle (PEP)* (see also section 2.1.1). It can also be seen that particles with purely fermionic exchange symmetry can not be in the same state from the following considerations: consider a system of 2 fermionic particles with 2 possible states. The unnormalized antisymmetric wave function is:

$$|\Phi_a\rangle = |\phi(1, 2)\rangle - |\phi(2, 1)\rangle \quad (2.42)$$

The wave function for the 2 fermionic particles being in the same state is (in this case in state 1):

$$|\Phi_a\rangle = |\phi(1, 1)\rangle - |\phi(1, 1)\rangle = 0 \quad (2.43)$$

So the antisymmetric wave function of 2 particles being in the same state is equal to 0. Therefore 2 fermionic particles can not be in the same state.

The relation described above between a particle's spin and its statistics is called the *Spin-Statistics Connection*. The anticommutation relations of creation ( $a^\dagger$ ) and annihilation ( $a$ ) operators for fermionic particles in states  $X$  and  $Y$  are:

$$\{a_X, a_Y\} = 0 \quad \{a_X^\dagger, a_Y^\dagger\} = 0 \quad \{a_X, a_Y^\dagger\} = \delta_{X,Y} \quad (2.44)$$

From 2.44 it can be seen that adding or removing 2 particles from a state results in 0 (as for example  $\{a_X, a_Y\} = a_X a_Y + a_Y a_X = 0$ ). Consequently not more than 1 particle can be in the same state for fermions. The action of these operators for fermionic particles on the unoccupied vacuum state  $|0\rangle$  and the state occupied by 1 particle  $|1\rangle$  can be written as

$$a|0\rangle = 0 \quad a|1\rangle = |0\rangle \quad a^\dagger|0\rangle = |1\rangle \quad a^\dagger|1\rangle = 0 \quad (2.45)$$

In the literature many proofs for the Spin-Statistic connection exist (e.g. [9], [10]). A clear set of assumptions for this proof was presented by Lüders and Zumino in [11]. The authors present 5 postulates plus gauge invariance as a foundation of their proof. These 5 postulates are:

- Invariance with respect to the proper inhomogeneous Lorentz group (which contains translations, but no reflections)
- Locality - 2 operators of the same field separated by a spacelike interval either commute or anticommute
- The vacuum is the state of the lowest energy
- The metric of the Hilbert space is positive definite
- The vacuum is not identically annihilated by a field

It is worth noting that the mentioned proof also holds for interacting fields. Another interesting point is that the Spin-Statistics connection does not hold for 2 spatial dimensions. The concept of *anyons*, a class of particles which does not follow bosonic or fermionic statistics, was presented in [12] in this context.

## 2.2. Theories of Violation of Spin-Statistics

There have been many attempts to find a theory of quantum mechanics which is consistent with a violation of Spin-Statistics. Here some important ones are reviewed.

### 2.2.1. Parastatistics

The first proper quantum statistical generalization of fermi and bose statistics was done by Green [13], [14]. He noticed that the commutator of the occupation number operator of the state  $X$ :  $N_X = a_X^\dagger a_X$  with the annihilation and creation operators is the same for fermions and bosons:

$$[N_X, a_Y^\dagger] = \delta_{X,Y} a_Y^\dagger \quad (2.46)$$

As a result, the number operator can be written as:

$$N_X = \frac{1}{2}[a_X^\dagger, a_X]_\pm + const \quad (2.47)$$

The  $\pm$  sign denotes the (anti-)commutator for the (bosonic) fermionic case. The expression for the transition operator  $N_{X,Y}$  which annihilates a particle in state  $Y$  and creates a particle in state  $X$  leads to the trilinear commutation relation <sup>3</sup> for parabose and parafermi statistics:

$$[[a_X^\dagger, a_Y]_\pm, a_Z^\dagger] = 2 \delta_{Y,Z} a_X^\dagger \quad (2.48)$$

These relations have an infinite set of solutions corresponding to each integer  $p$ . The integer  $p$  is the order of the parastatistics and gives the number of particles that can be in an antisymmetric state in the case of parabosons and the number of particles that can be in a symmetric state in case of parafermions. The case  $p = 1$  corresponds to normal fermionic or bosonic statistics. It was shown that the squares of all norms are positive for states satisfying Green's trilinear commutation relation. Nevertheless, the violations introduced by these statistics is large and no precision experiments are needed to rule them out.

### 2.2.2. The Ignatiev and Kuzmin Model and Parons

In 1987, A. Ignatiev and V. Kuzmin constructed a model of one oscillator with 3 possible states: a vacuum state with no occupancy, a one particle state and with a small amplitude parametrized by a  $\beta$  a state occupied by 2 particles [15]. The creation and annihilation operators connect these 3 states (analogous to 2.45) as:

$$a|0\rangle = 0 \quad a|1\rangle = |0\rangle \quad a|2\rangle = \beta|1\rangle \quad (2.49)$$

---

<sup>3</sup>A trilinear form is a function of 3 arguments, in which every argument enters only to first order.

$$a^\dagger |0\rangle = |1\rangle \quad a^\dagger |1\rangle = \beta |2\rangle \quad a^\dagger |2\rangle = 0 \quad (2.50)$$

They were able to give trilinear commutation relations for their oscillator. It is worth noting that the authors calculated the oscillations violating the PEP are suppressed by a factor proportional to  $\beta^2$  compared to oscillations that do not violate the PEP and vanish for  $\beta = 0$ . Following these ideas, Mohapatra and Greenberg ([14]) described this model as a modified version of the order-two Green ansatz. They introduced a parameter  $\beta$  giving a deformation of Green's trilinear commutators (see 2.48). For  $\beta \rightarrow 1$  the relations reduce to those of the  $p = 2$  parafermi field. For  $\beta \rightarrow 0$  on the other hand double occupancy is completely suppressed and fermi theory is obtained. Particles described by this theory were called *parons*. A state of 2 paronic electrons has the probability to be in a double occupancy state of  $\frac{\beta^2}{2}$ . It was shown by A. Govorkov in [16] that every alteration of Green's commutation relation (like the one discussed here) necessarily has states with negative squared norms. Thus the model of Igantiev and Kuzmin cannot be extended to become a true field theory.

### 2.2.3. Quons

The idea of a class of particles called *quons* was described by O. W. Greenberg [17]. The commutator algebra of quons can be obtained as the convex sum of the fermi and bose commutator algebras

$$\frac{1+q}{2}[a_X, a_Y^\dagger] + \frac{1-q}{2}\{a_X, a_Y^\dagger\} = \delta_{X,Y} \quad (2.51)$$

or

$$a_X a_Y^\dagger - q a_Y^\dagger a_X = \delta_{X,Y} \quad (2.52)$$

In equations 2.51 and 2.52 the parameter  $q$  was introduced, which interpolates between a fermionic ( $q = -1$ ) and a bosonic ( $q = 1$ ) commutation relation. For the quonic states to have positive squared norms, this parameter needs to be within  $-1 \leq q \leq 1$ . For  $q$  deviating from  $\pm 1$ , the multidimensional representations of the permutation group, which correspond to Young diagrams with more than one row/column, smoothly become more heavily weighted and have a non-zero probability of being realised. That means for a state with 2 particles, for which only completely symmetric and antisymmetric wave functions are possible, a density matrix <sup>4</sup> can be given to represent the mixture of the possible states in the form

$$\rho = \frac{1+q}{2} |\phi_s\rangle \langle \phi_s| + \frac{1-q}{2} |\phi_a\rangle \langle \phi_a| \quad (2.53)$$

---

<sup>4</sup>A density matrix describes a statistical ensemble of several quantum states. This is in contrast to a quantum mechanical mixture of a pure state, described by a state vector.

For fermionic quons, the factor  $q$  would be close to and slightly larger than -1. For bosonic quons, the factor  $q$  would be close to and slightly smaller than 1. When the theory of quonic fermions is related to paronic fermions, where the probability of a state with double occupancy is  $\frac{\beta^2}{2}$ , it follows that

$$\frac{\beta^2}{2} = \frac{1 + q_F}{2} \Rightarrow q_F = \beta^2 - 1 \quad (2.54)$$

Quonic particles clearly violate the Spin-Statistics connection. It is worth noting nevertheless, that several properties of relativistic theories do hold, like the CPT theorem for example. But as the Spin-Statistics connection does hold for relativistic theories with the usual properties, some property has to fail. This is the property of locality. It turns out that in this framework, observables separated by spacelike separation <sup>5</sup>, do not commute.

## 2.3. Tests of the Pauli Exclusion Principle

why test -> 1 okun, greenberg, jackson, Elliott -> division of experiments; other tests than VIP2

### 2.3.1. Remarks on testing the Pauli Exclusion Principle

The question might be asked as to why one should test the PEP and thereby the Spin-Statistics connection, if it can not be violated in a relativistic theory with the usual properties. O. W. Greenberg gives in [14] several “external motivations” which could lead to a possible violation of Spin-Statistics, namely:

- violation of CPT
- violation of locality
- violation of Lorentz invariance
- extra space dimensions
- discrete space and/or time

---

<sup>5</sup>Points with spacelike separation are not connected by a lightcone and are therefore not causally connected.

- noncommutative spacetime

As these items are subjected to active research, it seems plausible also to experimentally test the Spin-Statistics connection. Unfortunately, the level of a possible violation, if it is occurring, is unknown. Also there is no reason, why a possible violation should be as small as experiments find it to be. Another important point when testing the PEP is that one does not search for fermions which are “a bit” different. If this kind of slightly different fermions would exist, the lowest order pair production cross section would double [14]. This is clearly ruled out by experiments. Because of the indistinguishability of identical particles, all fermions should have the same possibility for an admixture of a symmetric state. This is reflected in the use of the density matrix for the description of states in the case of quons.

### 2.3.2. Experiments for testing the Pauli Exclusion Principle

According to S. R. Elliott, the various experiments testing the Pauli Exclusion Principle can be grouped into 3 classes [18], with respect to the kind of fermionic interaction they are investigating. 3 different types of interactions were given:

- Type 1: interactions between a system of fermions and a fermion that has not yet interacted with any other fermion
- Type 2: interactions between a system of fermions and a fermion that has not yet interacted with this given system
- Type 3: interactions between a system of fermions and a fermion within this system

These distinctions between different interactions are necessary due to the MG superselection rule (see also section 2.1.4). This rule forbids changes of the permutation symmetry of a quantum state in a system where the number of particles is constant. The important difference among these classes is that in a type 3 interaction, the superselection rule forbids a change in permutation symmetry as the investigated fermion already has a defined permutation symmetry with the surrounding system and the number of particles in the system does not change. Subsequently the different types of experiments will be discussed and examples will be given:

### Type 1 experiments:

The typical experiment of this type uses recently created fermions and lets them interact with the system under investigation. In 1948 Goldhaber and Scharff-Goldhaber [1] produced electrons with a  $\beta$  source and let them capture on Pb atoms. The authors idea was that if the electrons from the  $\beta$  source are not subject to the PEP in the electron shell of the Pb atoms, they could cascade to the ground state and thereby emit photons which would be detected. The lack of these photons was used to set an upper limit on the probability for the violation of the PEP. The fundamental point is that the electrons from the  $\beta$  source has not yet interacted with any system and is therefore necessarily new to the electronic system of the Pb atoms. As they are new to this system, they can form new quantum states with the Pb atoms. Forming states with a symmetric admixture is then not forbidden by the MG superselection rule. This is in particular also true, if the electronic state of the atom has previously been in a completely antisymmetric state. Other sources of recently produced fermions can also be pair-production processes and nuclear reactions.

### Type 2 experiments:

In this kind of experiments, fermions are brought to a system to interact with it. These fermions have not recently been created for type 2 experiments. But the fermions do not have previously interacted with the system. The typical experiment is the one conducted by Ramberg and Snow [2]. In this experiment, electrons were introduced to a Cu conductor via a current. These current electrons have no previous interaction with the atoms in the conductor. Therefore the same arguments apply as for type 1 experiments and the formation of a state with an admixture of symmetric exchange symmetry between the atoms of the conductor and a conduction band electron is not forbidden by the MG superselection rule.

In case of a symmetric admixture in quantum state formed between the atoms in the conductor and the current electrons, the current electron could cascade to the ground state, thereby emitting photons. The lack of detected photons was again used to set an upper limit on the probability for the violation of the PEP. An interesting point is the precise origin of the electrons in the conduction band. In an optimal setup, they are coming from a battery. This would guarantee the newness of the electrons. The drawback is that a high current is hard to maintain in this way. If the power of the current source comes from an AC grid the electrons in the conduction band of the conductor will comprise electrons from the conductor

itself and the circuitry connecting it to the power supply.

An interesting idea was put forward by E. Corinaldesi [19], who suggested that the PEP is not a kinematic principle but rather a time-dependent effect of interactions and that newly formed system may undergo PEP violating transitions, whose rate decreases in time. This suggestion could be tested with a type 2 experiment. In [20] it was suggested that this hypothesis can be tested by crossing an electron and a  $\text{Ne}^+$  ion beam and to monitor potential photons from PEP violating transitions.

### Type 3 experiments:

A type 3 experiment searches for a PEP violating transition in a stable fermionic system where the number of particles is constant. Notably the considered systems need to change their permutation symmetry in order to undergo these transitions. Therefore type 3 experiments violate the MG superselection rule and their outcome can not be compared to type 1 and type 2 experiments.

Nevertheless, many experiments of this kind have been conducted. Pioneers in this kind of experiment were Reines and Sobel [21]. They were looking for transitions of L-shell electrons to the already occupied K-shell in iodine atoms. The DAMA/LIBRA experiment conducted an analysis of their data regarding the same process [22]. Nuclear processes were also investigated regarding PEP-violating transitions, for example in [23] by the Borexino collaboration. The experimenters were looking for non-Paulian transitions of nucleons from the 1p to the 1s nuclear shell.

### Anomalous Structures

Another type of experiment is to look for anomalous nuclear and atomic structures. In [24] an experiment is reported where nuclear states with 3 nucleons in the 1s ground state are searched for. Non-Paulian atomic states of Be are explored in [25].

Some limits on the probability of a violation of the PEP are summed up in table 2.3.2.

Process	Type	$\frac{\beta^2}{2}$ limit	Reference
anomalous atomic transition	1	$3 \times 10^{-2}$	[1]
anomalous atomic transition	2	$4.7 \times 10^{-29}$	[4]
anomalous atomic transitions	3	$6.5 \times 10^{-46}$	[22]
anomalous nuclear transitions	3	$2.2 \times 10^{-57}$	[23]

The most stringent limit prior to the VIP2 experiment in a system circumventing the MG superselection rule (type 1 + 2 experiments) is set by the VIP experiment [4]. The experimental method of the VIP and VIP2 experiments will now be described.

## 2.4. The VIP2 experimental method

copper - element of group 11 like silver and gold - e- configuration source of electrons = current -> ez way to get electrons many; electrons in a conductor, fermi sphere, interactions; cascading process; new symmetry state

As was mentioned in section 2.3.2, the change of permutation symmetry of a quantum state is not forbidden by the MG superselection rule, when a fermion which is new to the studied system (e.g. atom, nucleus) interacts with it. These types of experiments were classified as type 1 and type 2. To the best of our knowledge, the most feasible way to introduce a large number of fermions into a system is by introducing a current into a conductor. The number of electrons introduced in this way is for 1 A  $\sim 10^{19}$  per second. While moving through the conductor with a velocity influenced by the applied electric potential, these electrons have a certain probability to interact with the atoms in the conductor. Due to this interaction, the electrons from the conduction band can form a new quantum state with the electrons in the atom. It is important to mention that these electrons did not have a defined symmetry with respect to the atomic electrons before this interaction happens, as they come from the current source outside of the conductor. This formation of a new quantum state is the reason why this kind of experiment does not violate the MG superselection rule. After the formation of the new state, the former current electron has the possibility to have symmetric permutation symmetry with respect to particle exchange with the other electrons in the electron shell if the PEP can be violated. This electron sees all the states occupied by the atomic electrons as empty and can occupy them. Therefore it will cascade down into the 1s ground state of the atom, thereby emitting photons as it loses energy. These photons are collected for some time with and without a

current. As there are no new electrons introduced during the measurement without current, there are also no photons expected in this time. This measurement is used to determine the background of the energy spectrum. From the difference between the energy spectra in the energy regions where one expects photons from the PEP violating transitions, one can calculate the probability for a violation of the Pauli Exclusion Principle in an atom, or set upper bounds for this probability.

For the VIP2 experiment the conducting material is copper ( Cu ). It has the atomic number 29 and is part of the group 11 in the periodic table of elements together with for example silver (atomic number 47) and gold (atomic number 79). These elements have in common that they are good conductors for electrical currents. Copper has a resistivity at room temperature of  $1.68 \times 10^{-8} \Omega m$ , silver has  $1.59 \times 10^{-8} \Omega m$  and gold has  $2.44 \times 10^{-8} \Omega m$ , making silver the best conductor of the 3. But due to its low cost, copper was the obvious choice for this experiment. The mentioned elements are good conductors due to the unpaired electron in the outermost s-shell. The electronic configuration for copper for example is [Ar]  $3d^{10}4s^1$ . The Fermi energy <sup>6</sup> overlaps the 4s orbital [26]. It is a broad band <sup>7</sup> which resembles the dispersion relation of free electrons. At finite temperature the electrons of the 4s orbital can move freely in this band (i.e. change their momentum) and be the carrier of the current.

The energies of the aforementioned cascading process were calculated for copper atoms in [27] using a self-consistent multiconfiguration Dirac-Fock (MCDF) approach. In this case self-consistent is best explained with the help of figure 2.2. It means after calculating the potential from a charge density at any step and solving the Schrödinger equation with it, the charge density calculated from the Schrödinger equation needs to be the same as the initial charge density. The term “multiconfiguration” comes from the fact that the total wave function is described as a linear combination of configuration state functions, which are related to a specific configuration of electrons. Using the Dirac-Fock approach as opposed to the Hartree-Fock means that relativistic effects are accounted for. The relativistic Breit-Dirac Hamiltonian is used which takes into account all electromagnetic interactions of spin  $\frac{1}{2}$  particles including spin-orbit coupling and retardation effects. After self-consistency is achieved, the total energy is corrected by vacuum polarization effects (self energy and vacuum polarization). In the whole procedure the “no pair” approximation is applied which explicitly excludes electron positron pairs.

---

<sup>6</sup>The Fermi energy is the energy of the highest occupied energy state of a system at a temperature of 0 K.

<sup>7</sup>An energy band in a solid is a region of allowed states in a  $E(\vec{k})$  diagram. Here  $E$  is the energy and  $\vec{k}$  is the wave vector.

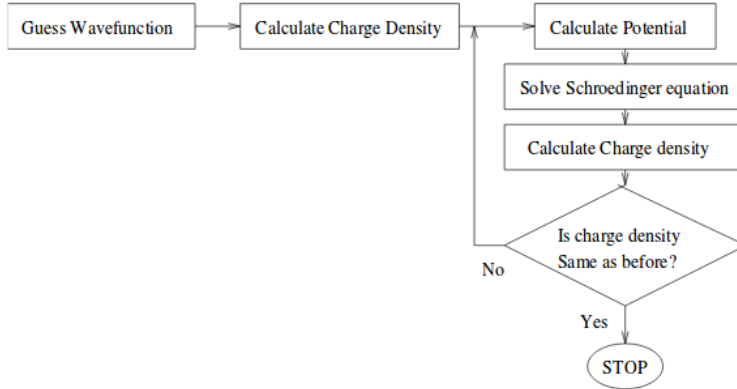


Figure 2.2.: A self-consistent algorithm for calculating the energy of atomic states.

The original code for these calculation which was adapted is described in [28]. It calculates the energies of atomic states in an electronic shell in which all but one electron have antisymmetric exchange symmetry. These states violate the PEP. The working principle of the calculation was described as 3 step process in [29]:

- Step 1: The functional form of the wave function is selected and defined in terms of certain functions (mostly hydrogen-like wave functions) which are combined with certain parameters.
- Step 2: An expression for the total energy is derived in terms of these functions and parameters.
- Step 3: The variational principle is applied and equations are derived for the valid solutions that are the functions that leave the total energy stationary. In this step self-consistency is checked.

The total wave function must then also obey the Hartree-Fock assumptions, for example that the wave function is antisymmetric with the exception of the one electron which has symmetric exchange symmetry. Furthermore the total wave function needs to be an eigenfunction of the  $L^2, L_z, S^2$  and  $S_z$  operators. The results of these calculations for copper are summed up in table 2.1.

It is interesting to note that while for normal transitions the  $K_{\alpha 1}$  transitions has twice the intensity of  $K_{\alpha 2}$ , the corresponding PEP-violating  $K_{\alpha 2}$  has a slightly higher intensity. This is why for future calculations the energy value of the PEP forbidden  $K_{\alpha 2}$  line of 7729 eV will be used. Furthermore as the transition rate of the  $K_{\beta}$  is lower by one order of magnitude, the primary focus of the analysis will be on the  $K_{\alpha}$  transitions. Another thing to note as due to the angular momentum

Transition	Transition energy - PEP violating (eV)	Transition energy - normal (eV)	Radiative transition rate ( $s^{-1}$ )	Multipole Order
$2p_{\frac{3}{2}} \rightarrow 1s_{\frac{1}{2}}$ ( $K_{\alpha 1}$ )	7748	8048	$2.56 \times 10^{14}$	E1 + M2
$2p_{\frac{1}{2}} \rightarrow 1s_{\frac{1}{2}}$ ( $K_{\alpha 2}$ )	7729	8028	$2.63 \times 10^{14}$	E1
$3p_{\frac{3}{2}} \rightarrow 1s_{\frac{1}{2}}$ ( $K_{\beta 1}$ )	8532	8905	$2.68 \times 10^{13}$	E1 + M2

Table 2.1.: Transition rate and energies for PEP violating transitions in copper calculated with the MCDF algorithm [27].

selection rules <sup>8</sup>, the 2s - 1s transition is forbidden, which also holds true for PEP forbidden transitions.

The difference in the transition energies between the normal K-lines and the PEP forbidden K-lines listed in table 2.1 can be explained with figure 2.3. On the left

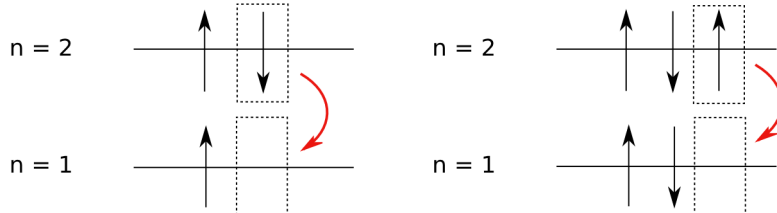


Figure 2.3.: Scheme of normal 2p to 1s transition (left) and a 2p to 1s transition which is violating the PEP (right).

side of the figure a normal 2p to 1s transition is shown. In this transition an electron from the 2p shell fills a vacancy in the 1s ground state, thereby losing 8048 eV of energy in the form of a photon. On the right side the corresponding PEP violating transition is shown. The electron undergoing the transition cascades down from the 2p into the 1s shell, but in this case, the 1s shell is occupied with 2 electrons.

<sup>8</sup>The conservation of angular momentum demands  $|J_i - J_f| \leq \lambda \leq J_i + J_f$ , where  $J_{i,f}$  are the initial and final total angular momenta and  $\lambda$  is the photons angular momentum.  $\lambda = 0, 1, 2, \dots$  for electric and magnetic monopole, dipole, quadrupole, ... transitions. The change of parity for electric transitions is  $(-1)^\lambda$  and for magnetic transitions it is  $(-1)^{\lambda+1}$ , which ensures the conservation of overall parity. The parity of a state is  $(-1)^L$ , so it does not change from 2s to 1s. As for electric dipole transitions the parity needs to change, it is electric dipole forbidden.

This is only possible because of the symmetric admixture in the symmetry of the wave function. Due to the fact that the 2 electrons in the 1s ground state shield the core potential more than the 1 electron in the case of the normal transition and thereby reducing the effective nuclear charge, the transition energy is lower for this transition. In the case of the  $K_{\alpha}$  transition for copper, the difference in energy is around 300 eV.

# 3. The Measurement Setup

description of the setup: sdd working principle etc, copper target, scintillator working principle etc, sipm working principle etc, working principle of the cryogenics used; description of sdd and sipm preamplifiers?; x ray tube + fe source; actual setup configuration; description of the daq: modules used (adc, qdc, tdc), timing, trigger, gates; Slow Control hardware/software!

As was mentioned in chapter 2, the core functionality of the VIP2 experiment is to measure energy spectra in the energy region where the PEP violating  $K\alpha$  transition is expected. For this purpose Silicon Drift Detectors were used. They offer an energy resolution which is good enough for our purpose of separating the energy peak coming from photons from allowed transitions from those coming from PEP-forbidden transitions, which are separated by 300 eV. Furthermore they offer a time resolution  $< 1 \mu\text{s}$ . This allows the use of an active shielding system, which consists of 32 plastic scintillator bars arranged around the copper target and the SDDs. They are read out by Silicon Photomultipliers. The working temperature of the SDDs was around 100 K. Their temperature was kept constant by a system composed of a helium compressor liquefying argon, which in turn cooled the detectors. A data acquisition and a slow monitor system were in place to collect data and monitor crucial parameters of the experiment. A schematic drawing of the experiment is shown in figure 3.1. All these components will now be described in detail.

## 3.1. Silicon Drift Detectors and copper target

used for..., working principle, mounting in the setup, energy resolution - fano + constant noise?; put the physics of photon absorption to the spectrum fit

Silicon Drift Detectors (SDDs) are used in the VIP2 experiment as X-ray detectors. They are mounted as close as 5 mm away from the Cu target in the setup, to reach maximum solid angle coverage.

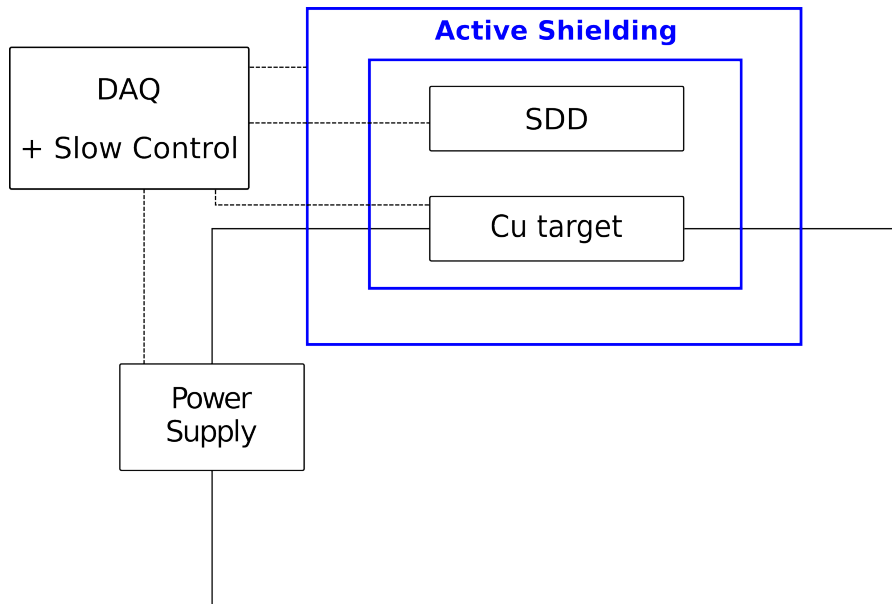


Figure 3.1.: Schematic drawing of the VIP2 experiment.

The Cu target consists of 2 strips with a length of 7.1 cm, a width of 2 cm and a thickness of 50  $\mu\text{m}$ . The strips are connected to a current supply via Cu connectors. In between the 2 strips runs a water cooling line to keep them at a constant temperature even with a high current flowing through them. One SDD array with 3 individual cells is mounted on each side of the target strips.

### 3.1.1. Working principle

The working principle of Silicon Drift Detectors is based on sideward depletion, which was first introduced in [30]. A schematic drawing of an SDD used for the VIP2 experiment is shown in figure 3.2. On a cylindrical n-type<sup>1</sup> silicon wafer circular p<sup>+</sup>-type silicon contacts are implanted on one flat surface. These contacts are used to apply an increasing reverse bias in order to fully deplete the wafer. The radiation entrance windows is on the opposite side of the concentric contacts and consists of a homogeneous shallow junction, which gives homogeneous sensitivity over the whole surface. When ionizing radiation hits the silicon wafer, electron-hole pairs are generated. The free electrons fall to the lowest point of the potential

---

<sup>1</sup>n-type semiconductors are doped with elements that are pentavalent, like phosphorus. This results in an excess of electrons. p-type semiconductors are doped with trivalent elements like boron, which results in an excess of holes.

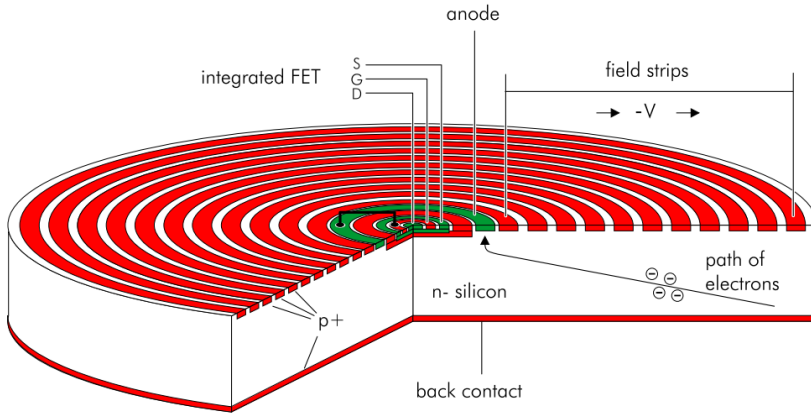


Figure 3.2.: Scheme of a Silicon Drift Detecor [31].

produced by the concentric electrodes. This lowest point is the anode consisting of a ring close to the middle of the wafer. The amount of electrons generated in the wafer and collected by the anode is proportional to the energy of the radiation. By measuring the amount of charge collected this energy can be calculated. The small size of the anode ensures a small anode capacitance, which is almost independent of the size of the detector [32] and only proportional to the anode's size. As some sources of noise are proportional to the capacitance ????, this reduces the noise and allows shorter shaping times <sup>2</sup> which in turn allows high count rates. As a first stage of amplification, a field effect transistor (FET) <sup>3</sup> is integrated in the chip and connected to the anode by a metal strip. Thereby the capacitance between detector and amplifier is minimised and electric pickup noise is mostly avoided. The anode is discharged continuously. This avoids regular dead times of the detector by a repeating reset mechanism.

### 3.1.2. SDD specifications for the VIP2 experiment

sources of noise -> expected energy and time resolution as a function of temperature

The manufacturer of the employed detectors (PNSensors) produced a manual,

---

<sup>2</sup>Long shaping times can be used in order to cancel out noise.

<sup>3</sup>A field effect transistor controls the conductivity between the source (S) and the drain (D) via an electric field between the body and the gate (G) of the device.

from which the information in this section is mainly taken [31]. The SDDs employed in the VIP2 experiment are 2 arrays with 3 detector cells each. Each cell has an active area of  $1 \text{ cm}^2$  shaped like a “rounded square” with a diameter of 10.3 mm and a corner radius of 2 mm. The maximum drift path length for electrons originating in a corner is 6.4 mm. The cells have a thickness of 450  $\mu\text{m}$ , which ensures a absorption of  $\sim 99\%$  of 8 keV (Cu K $\alpha$  line) X-rays. The 3 cells in an array share a common outermost strip (Rx), a common bulk contact (outer substrate - Os) and common guard ring systems on both sides of the chips. Each cell has a readout structure in its center and individual back contact (Bc) and separation mesh (back frame, Bf) contacts. The bonding and the way the voltages were adjustable were modified slightly for the VIP2 experiment. The important contacts and the way the respective voltages are adjustable (all SDDs common, all SDDs in an array, each individual SDD cell) are shown in table 3.1. Plots of the front and the back side of the arrays are shown in 3.3 and 3.4. There is a

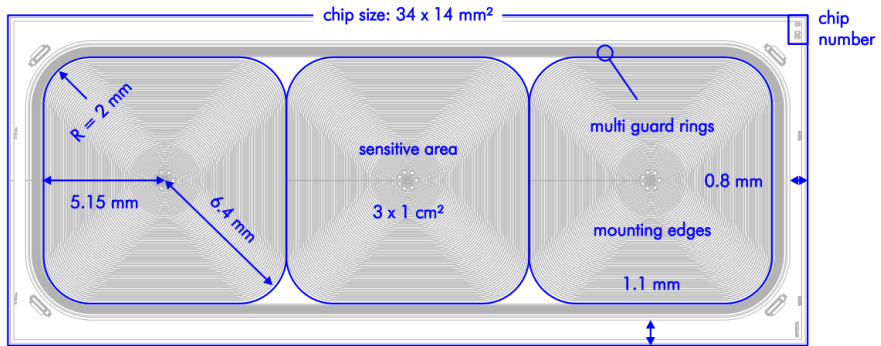


Figure 3.3.: Front side of the SDD array of the VIP2 experiment [31].

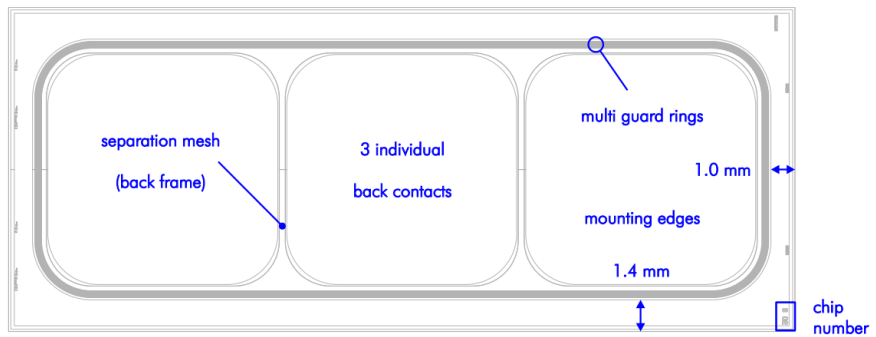


Figure 3.4.: Back side of the SDD array of the VIP2 experiment [31].

total number of 74 concentric electrodes, where the innermost 23 are circular and

the ones more on the outside are linear in vertical and horizontal direction with rounded edges. The first and the last ring are biased externally, the others are supplied via a resistive voltage divider.

Contact Name	Abbreviation	Bonding	Nominal Value [31]
Outermost strip	Rx	Common	-240 V
Innermost strip	R1	Common	-15 V
Outer substrate	Os	Common	GND
Inner substrate	Is	Common	GND
Entrance Window	Bc	Cell	-120 V
Separation Mesh	Bf	Array	-140 V

Table 3.1.: Some important contacts of the Silicon Drift Detectors used for the VIP2 experiment.

### 3.1.3. Silicon Drift Detectors performance characteristics

The energy and time resolution as well as scale linearity are crucial factors in the performance of the SDDs. The possibility of a high event rate would be another point to consider, but as this is not an issue for the VIP2 experiment with count rates of  $\sim 2$  Hz, this point will not be discussed.

The detector linearity is the ratio between produced electron-hole pairs and energy as a function of energy. In case the whole energy of the incident radiation is deposited in the detector and no losses during the charge transport, the number of electrons arriving at the anode only depends on the energy. Consequently the detector response should be perfectly linear with energy.

An advantage of semiconductor detectors with respect to gaseous detectors is the lower energy needed to create an electron-hole pair. At 77 K, this energy is 3.81 eV [33], which is independent of the type and energy of the incident radiation. The amount of charge carriers produced by the same radiation will therefore be one order of magnitude higher than in gaseous detectors. Therefore, semiconductors provide a greatly enhanced energy resolution. On the other side, the energy resolution is limited by noise. One part is the so-called fano noise. It results from a non-constant amount of electron-hole pairs produced for different events with the same energy. The fano factor is defined as:

$$F = \frac{\sigma^2}{\mu} \quad (3.1)$$

Here  $\sigma^2$  is the variance of the number of produced electron-hole pairs and  $\mu$  is the average of the number of electron-hole pairs. It is not dependent on energy and for Silicon the value is estimated to be  $F = 0.12$  [33]. Another source of noise is the leakage current, which is a small fluctuating current flowing through semiconductor junctions in case of an applied voltage. The fluctuation in the current appears as noise in the detector. One source of leakage current are thermally created electron-hole pairs originating from recombination and trapping centers in the depletion region. These centers result from impurities in the crystal. This part of the noise can be suppressed by lowering the temperature. Another source of leakage current are surface currents.

In order to reach the best possible energy resolution, an Fe-55 source <sup>4</sup> is installed in the VIP2 setup. The photons from the source hit the SDDs directly and also induce K $\alpha$  transitions in a titanium foil located between the source and the detector. These 2 photon sources enable continuous calibration of the energy scale and thereby minimize peak drift effects and optimize the energy resolution.

The time resolution of the SDDs is determined by the drift time of the electrons from their origin to the anode. In [31] the maximum drift time at 150 K for the type of detector used in the VIP2 experiment is estimated to be 600 ns. Due to the temperature dependence of the electron mobility (e.g. increased phonon scattering), the time resolution generally gets worse with rising temperature.

## 3.2. Active Shielding

how light propagates -> reflectivity -> wrapping; physics of interaction with different radiations maybe in simulations

The active shielding system has the purpose of rejecting SDD events caused by external radiation. This means that whenever a signal in the SDDs is in coincidence with a signal from the scintillators, it can be rejected. The active shielding consists of 32 scintillators read out by 2 Silicon Photomultipliers (SiPMs) each, which are assembled around the copper target and the SDDs. A render of the setup including the active shielding system enclosing the target is shown in figure 3.5.

---

<sup>4</sup>An Fe nucleus with 26 protons and 29 neutrons decays via electron capture to Mn-55 with a half-life of 2.737 years. This results in the emission of a photon or an Auger electron.

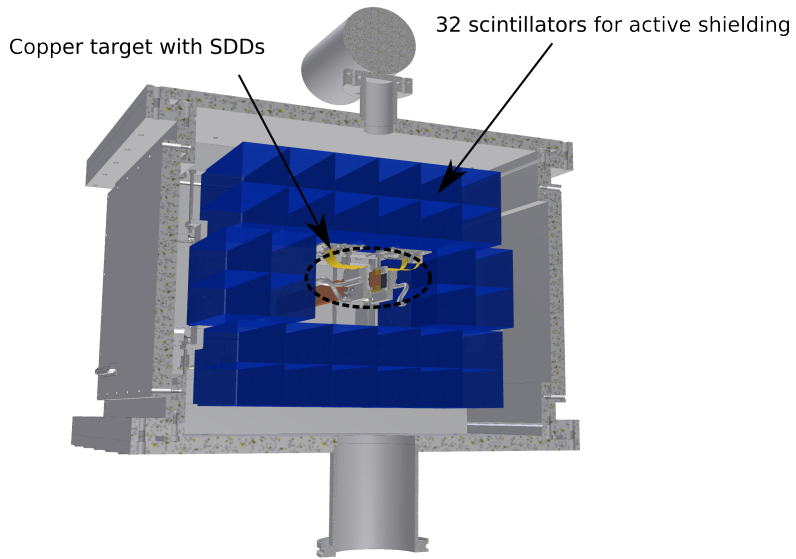


Figure 3.5.: Active shielding system of the VIP2 experiment consisting of 32 scintillators.

### 3.2.1. Scintillators

Scintillators are materials that emit photons after they are excited by ionizing radiation. The scintillators used in the VIP2 experiment are plastic scintillator bars of the type EJ-200 produced by Eljen Technologies. Their dimensions are 38 mm x 40 mm x 250 mm. The base polymer is polyvinyl toluene [34]. When ionizing radiation passes through the scintillator, electrons in the valence band in so-called molecular orbits are excited [33]. Subsequently the excited states loose their energy via the emission of a photon. A flour is suspended in the polymer matrix to absorb the UV radiation and re-emit it at visible wavelengths. The wavelength of maximum emission is then 425 nm (blue light) and the pulse width is 2.5 ns (FWHM) [34]. The scintillation material has a refractive index of 1.58, meaning that total internal reflection can occur for photons with a flat impact on the surface. Nevertheless light can also escape the scintillator if the impact angle is too steep. To increase the light collection on the SiPMs, the scintillators were wrapped in reflective aluminum foil to reflect stray photon back into the scintillator, while leaving a small air gap in between the foil and the scintillator. To minimize the influence of photons from the environment hitting the SiPMs, a layer of sticky black tape was wrapped around the aluminum foil.

### 3.2.2. Silicon Photomultipliers

A Silicon Photomultiplier consist of an array of semiconductor pn junctions with a high reverse bias. For the VIP2 experiment, we use the  $3 \times 3 \text{ mm}^2$  ASD-SiPM3S-P50 SiPMs manufactured by AdvanSiD. On one end of each scintillator bar, 2 SiPMs are attached with optical glue ??? and connected in series. In that way, as opposed to reading both SiPMs individually, the signal to noise ratio and the time resolution can be improved ??. One SiPM consists of 3600 sequentially connected Silicon avalanche photodiodes (APD) with an area of  $50 \times 50 \mu\text{m}$  each. All of them are operated in Geiger mode (an analogy to the Geiger counter), meaning that the reverse bias voltage is higher than the breakdown voltage<sup>5</sup>. In this mode, the generation of one charge carrier causes an avalanche of charge carriers due to impact ionization. The first charge carrier can be produced by an incident photon undergoing the photoeffect. In the case of the VIP2 experiment, this photon comes from the scintillator. The energy of the optical photons from the scintillator (425 nm  $\sim 2.9 \text{ eV}$ ) is enough to generate an electron-hole pair. The spectral response range for the SiPMs used for VIP2 is 350 nm - 900 nm [35], overlapping with the photon spectrum of the scintillator. One APD by itself is a digital device, as it can only decide if a photon hit it or not. Reading all APDs in a SiPM at the same time gives then an analog signal.

The time resolution of a system of scintillator read out by SiPMs is typically on the order of a few ns. This means that it is negligible compared to the time resolution of the SDDs, which is of the order of a few 100 ns.

## 3.3. Cooling system

he compress: compresses (9.8 bar  $\rightarrow$  22 bar) and cools (warms up due to compression) (to room temp or so) the he gas; also filters out oil mist in the gas in an adsorber and an oil separator  $\rightarrow$  + PID control

The Silicon Drift Detectors used for the VIP2 experiment have a working temperature of around 150 K [31]. To reach this temperature, a system of a helium compressor coupled to a pulse-tube refrigerator is used with helium gas as a working medium. The cooling power produced by this system is used to liquefy Argon, which then flows past the SDDs. Thereby it evaporates and cools the detectors

---

<sup>5</sup>The breakdown voltage of a diode is the minimum reverse bias voltage to make the diode conductive.

down.

As a helium compressor a CNA-21A helium compressor from SHI - (Sumitomo Heavy Industries -) cryogenics was used. This compressor gets  $\sim 9.8$  bar helium gas at room temperature from the cold head. This gas is then compressed to  $\sim 22$  bar and cooled back down to room temperature after it was heated due to the compression. The compressor is air-cooled meaning the helium gas flows through a heat exchanger after compression which is cooled by blowing air with a fan through it. The high pressure helium gas at room temperature is then supplied to a pulse tube refrigerator of the Gifford-McMahon type. The working principle of this type of refrigerator is shown in figure 3.6. The high pressure helium gas is connected

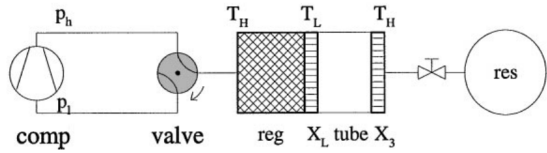


Figure 3.6.: Schematic drawing of a pulse tube refrigerator of the Gifford-McMahon type [36].

to the RP-2620A coldhead which is also manufactured by SHI - cryogenics. The cold head has a valve on its side close to the helium compressor. This valve connects the refrigerator to the high and the low pressure side of the compressor in an alternating way. Coming from the high pressure side of the compressor, the gas first hits a regenerator, at a high temperature ( $\sim$  room temperature)  $T_H$ . After the regenerator, there is a heat contact  $X_L$  to the medium to be cooled at the lower temperature  $T_L$ . Thereafter follows the pulse tube where the gas is thermally isolated (adiabatic) and therefore the temperature of the gas depends on its pressure. After the pulse tube a thermal contact to the surroundings is installed. The whole gas volume is coupled to a gas reservoir via a flow resistive valve. The heat exchangers, the regenerator and the pulse tube are suspended in vacuum of  $\sim 10^{-5} - 10^{-6}$  mbar.

When the high pressure helium gas flows through the regenerator, it is cooled down to  $T_L$  and the regenerator is warmed up to  $T_H$ . The gas enters the pulse tube at  $T_L$ . Then the pressure is switched to the low pressure of around 10 bar in our case, and the gas flows out of the tube. But due to the lower pressure, the temperature in the tube is now lower than  $T_L$ . The gas now flows through the thermal contact  $X_L$ . It cools the contact and thereby effectively cools the argon gas  $X_L$  it is in thermal contact with. The helium gas then flows through the regenerator at exactly  $T_L$ , cooling it to this temperature. The opposite effect occurs at the temperature  $T_H$  at  $X_3$ , where heat is dissipated to the environment.

The coefficient of performance (ratio between cooling power and compressor power) for an ideal pulse tube refrigerator is  $\frac{T_L}{T_H}$ , which is lower than the one of a Carnot process  $\frac{T_L}{T_H - T_L}$  due to losses in the valve [36].

The cooling power of the pulse tube refrigerator at  $X_L$  is used to cool down an aluminum target through which the argon gas flows. The argon condenses and flows down a pipe which runs past the SDDs, cooling them to their working temperature. Thereby the argon evaporates. Afterwards it is cooled again by the pulse tube refrigerator. A picture of the SDDs with the argon cooling line and a readout board is shown in figure 3.7.

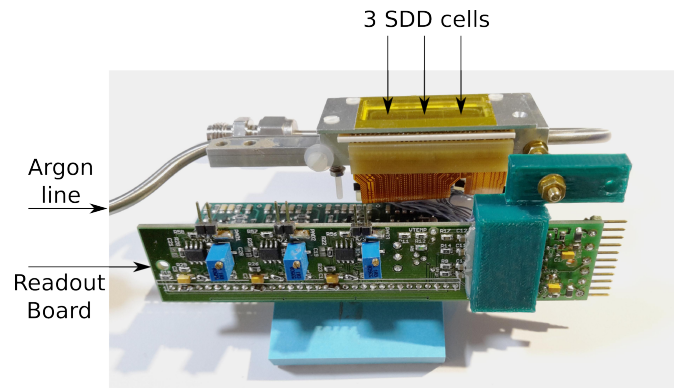


Figure 3.7.: The SDDs with the argon cooling line and the readout board.

The cooling of the pulse tube refrigerator is counteracted by a heating wire controlled by a LakeShore 331 temperature controller. This is done in order to be able to control the temperature of the argon by adapting the heating power. Changes in argon temperature can in this way be compensated with the PID (Proportional Integral Differential) control of the LakeShore 331 on a very short timescale. The vacuum necessary to maintain the necessary cryogenic temperatures is maintained by 2 turbo pumps connected to a common prepump.

## 3.4. Data acquisition and slow control systems

### 3.4.1. Signal readout and data acquisition

vme readout; simplified logic without timing = trigger; preamp board?; shaping time and gain of SDDs?; thresholds of sipms - maybe only that we can set them -

how big they are -> out into chapter test measurements;

After a first stage of amplification in the preamplifier board in the vacuum chamber, the signals of the 6 SDDs go into a programmable CAEN 568B spectroscopy amplifier. The fast “FOUT” signal goes to a discriminator for making a trigger. An OR of all 6 discriminated SDD signals is going to a CAEN V1190B TDC (Time to Digital Converter). The programmable “OUT” output of the amplifier is used for spectroscopic signal analysis. The spectroscopic signal is fed into a CAEN V785 peak sensing ADC (Analog to Digital Converter) for digitalizing the signal.

The signal from the 2 SiPMs from each of the 32 scintillators is amplified in a preamplifier board in the vacuum chamber. The analog signal is split thereafter, with one part going to a programmable Constant Fraction Discriminator (CFD) to make a timing signal and the other going to a CAEN V792 QDC (Charge to Digital Converter). Referring to figure 3.5, the 32 scintillators can be grouped into one “outer” one “inner” layer, and more specifically into 8 sub-layers with the indication of their position relative to the target (e.g. “top outer” layer indicates the 8 scintillators above the target, which are closer to the setup box). A signal of one of these layers is an OR of all the discriminated SiPM signals in this layer. The signal of each of these 8 sub-layers and an AND of the outer and inner layer is sent to the TDC.

The digital signal from the discriminators is used for making a trigger for the TDC, ADC and QDC modules. The trigger logic is shown in figure 3.8. It consists of the OR of all 6 SDDs making an OR with the inner AND outer scintillator layer. The AND of the inner and outer scintillator layer triggers on cosmic radiation or

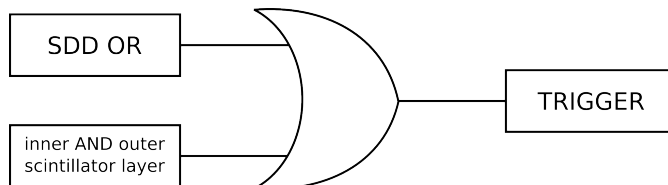


Figure 3.8.: Trigger definition of the VIP2 experiment.

any radiation which produces a detectable signal with high probability in every scintillator it passes through. The OR of the SDD signals includes every SDD event above a certain energy threshold. Also in the case of SDD only trigger (no scintillator AND), the signals (or lack thereof) of all 8 scintillator layers is recorded in the TDC.

The data from ADC, QDC and TDC are read out via a CAEN V2718 VME - PCI

bridge to a CAEN A2818 PCI controller. A LabView program is communicating with this controller to record and store the data in binary form.

### 3.4.2. Slow control

all the values read out/ controlled by slow, and how they are read; also with plugbars

The slow control is a system to monitor and control important parameters of the experiment. A schematic drawing of its layout is shown in figure 3.9. The central

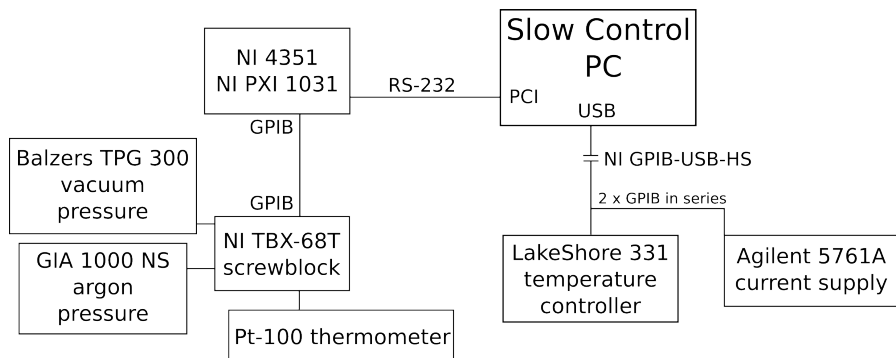


Figure 3.9.: A schematic layout of the slow control system of the VIP2 experiment.

point of the system a PC running a Visual C++ program which communicates with the different sensors and devices via a GPIB and a USB interface and stores the parameter values. The PC can be accessed remotely to control parameters and transfer the stored data. The USB interface is on the one hand connected to a LakeShore 331 temperature controller which regulates the heating of a wire which counteracts the cooling of the cold head and thereby regulates the argon temperature. On the other hand it is connected to an Agilent 5761A current supply which provides the current through the copper target. The GPIB interface is connected to a National Instruments (NI) PXI 1031 chassis with a NI PXI 4351 board. This is then connected via GPIB to a NI TBX-68T screwblock which receives analog signals from several sources, which correspond to pressure and temperature at different points in the setup. Temperature information comes from Pt-100 resistance thermometers and pressure readings come from a cold cathode<sup>6</sup> for low pressure and piezoresistive sensors<sup>7</sup> for high pressure. A list of all

<sup>6</sup>A cold cathode generates electrons via the discharge of a high voltage. The electrons ionize the gas and the number of produced ions is proportional to the gas pressure.

<sup>7</sup>The piezoresistive effect causes the resistance of a material to change under mechanical

parameters that can be measured and controlled with the slow control system can be found in table 3.2.

All the values listed in this table are stored periodically. An emergency system was in place which periodically checks the values recorded by the slow control. In case specific values exceed certain thresholds, crucial systems like the turbomolecular pumps and the SDDs could be turned off automatically. This was done by the communication with an Energenie EG-PM2-LAN plug which allows the automatic power shutdown of these devices which were attached to it.

---

strain.

Value to measure / control	Measured / Controlled by	Primary readout device	Adjustable
Room temperature	Pt-100	NI PXI 4351	No
Copper bar external temperature	Pt-100	NI PXI 4351	No
Copper bar internal temperature	Pt-100	NI PXI 4351	No
Water cooling pad temperature	Pt-100	NI PXI 4351	No
PCB board 1 temperature	Pt-100	NI PXI 4351	No
PCB board 2 temperature	Pt-100	NI PXI 4351	No
SDD 1 temperature	Pt-100	NI PXI 4351	No
SDD 2 temperature	Pt-100	NI PXI 4351	No
Argon upper line temperature	Pt-100	NI PXI 4351	No
Argon lower line temperature	Pt-100	NI PXI 4351	No
Argon target temperature	Pt-100	NI PXI 4351	No
Argon gas temperature	Pt-100	NI PXI 4351	No
Vacuum pressure	Balzers IKR 050 cold cathode	Balzers TPR-010	No
Argon gas pressure	Keller PAA-21-10	GIA 1000 NS	No
Heater output power	LakeShore 331	LakeShore 331	No
Heater PID settings	LakeShore 331	LakeShore 331	Yes
Argon gas set temperature	LakeShore 331	LakeShore 331	Yes
Current through copper	Agilent 5761A	Agilent 5761A	Yes

Table 3.2.: Summary of parameters measured and controlled by the slow control system.

# 4. Simulations

geant4 simulations of: the background rejection ratio for cosmics and for gammas; the energy deposition of MiPs in scintillators; the efficiency determination for detecting photons coming from PEP violating transitions

For the purpose of evaluating and verifying several experimental parameters, the complete setup has been modeled in the Geant4 framework [37]. The utilized version of the framework is Geant4.10.2 . All components of the setup were considered in the simulations including the SDDs with metal frames, the copper target and the copper current supply cables, the scintillators and the calibration foils as well as the aluminum vacuum box. The PENELOPE (PENetration and Energy LOss of Positrons and Electrons) model was chosen over the LIVERMORE model for electromagnetic processes. As atomic de-excitation processes were important, fluorescence, auger electron emission and PIXE (Particle induced X-ray emission) were turned on. The simulations were conducted by the collaborator Shi Hexi. A render of the setup is shown in figure 4.1.

## 4.1. Detection Efficiency

One objective of the simulation was to determine the efficiency of the setup. The efficiency is in our case defined as the probability for an X-ray coming from a PEP violating transition (i.e. a photon with an energy of 7.7 keV) originating in one of the two target strips to be detected in a SDD. Two factors contribute to the efficiency. On the one hand the solid angle coverage of the copper target by the SDDs limits the efficiency. Taking into account the fact that the aluminum pad for water cooling between the two copper foils absorbs  $\sim 100\%$  of these photons, the solid angle can be estimated to be  $\sim 10\%$  (from the ratio between the area of the target and the area of the SDDs). On the other hand some photons are lost by interactions with the 50  $\mu\text{m}$  Cu target. Here photoabsorption has the by far largest contribution to this loss. This contribution can be estimated with the attenuation of photons going through half of the target (25  $\mu\text{m}$ ) which is about 25

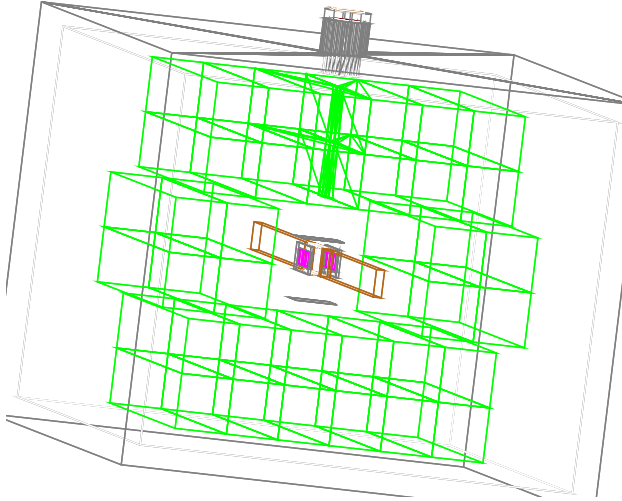


Figure 4.1.: View of the the VIP2 setup in a Geant4 MC simulation.

%. This gives an estimation for the whole efficiency of about 2.5 %.

To determine the efficiency with a simulation,  $10^6$  photons with 7.7 keV were simulated with their starting positions randomized in the copper target and their starting directions randomized over  $4\pi$  solid angle. The result of the simulation is shown in figure 4.2. In the figure all original vertices in one copper target strip (starting points - brown) of photons which deposit all their energy in the SDDs are shown. The last vertices (end point of the track - purple) where the photons lose their energy in the SDDs is also shown. Only photons are counted which deposit all their energy of 7.7 keV in the SDDs. It is evident from the figure, that most photons which are detected by the SDDs originate in the part of the 7.1 cm long target closer (“beneath” in the figure) to the SDDs. This can be explained with the larger solid angle under which these photons see the detector. Only one side of the simulation result is shown in the figure, as the setup is symmetric and the other side gives the same result. From the  $10^6$  photons starting from the target,

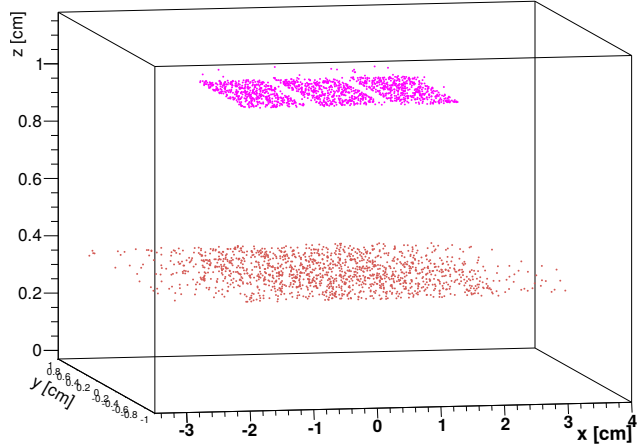


Figure 4.2.: Starting (brown) and end (purple) points of photons originating from the Cu target and hitting the SDDs.

18,200 were detected by the SDDs. This results in efficiency of 1.82 %, which is close to the estimation of 2.5 % and therefore a plausible result.

## 4.2. Cosmic Ray Background

Cosmic radiation seen at the surface of earth primarily consists of muons [38]. The origin of this radiation is so-called primary cosmic radiation consisting of nuclei which are part of stellar power generation such as hydrogen and helium nuclei. These particles hit earth's atmosphere mainly generating mesons, which then decay into the cosmic radiation seen at the surface of the earth (e.g. muons). The rate of muons integrated over the whole solid angle is  $\sim 1 \text{ cm}^{-2} \text{ min}^{-1}$  [38]. For the simulation,  $10^7$  muons were generated in an area of  $50 \text{ cm} \times 35 \text{ cm}$  which had a distance of 20 cm to the target. The particles had 270 GeV energy and their directions were randomized in the lower half-sphere. This energy was chosen as it was reported as the mean energy of the muon spectrum at LNGS in [39]. With the above mentioned rate this corresponds to the background of  $\sim 4$  days. This part of the background only plays a role in the measurements above ground, as it is reduced at the underground laboratory LNGS by several orders of magnitude. The goal of these simulations was to estimate the probability of the rejection of muons by scintillator veto and to estimate the signal rate from this source in the scintillators and SDDs.

The energy deposit in each scintillator summed up over all scintillators is shown in figure 4.3. A pronounced peak at  $\sim 8$  MeV deposited energy is visible. With a thickness of a scintillator of 4 cm, this corresponds to an energy loss of  $2 \frac{\text{MeV}}{\text{cm}}$ .

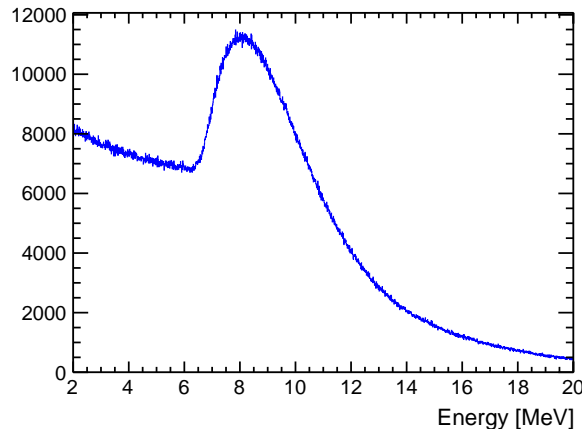


Figure 4.3.: Energy deposit of 270 GeV muons in plastic scintillators.

Furthermore, the trigger rate of the scintillators can be estimated from the rate of  $1 \text{ cm}^{-2} \text{ min}^{-1}$  to be  $\sim 1.67 \text{ s}^{-1}$  per scintillator. The energy deposit in the SDDs is shown in figure 4.4. The peak in deposited energy is in this case at around 300

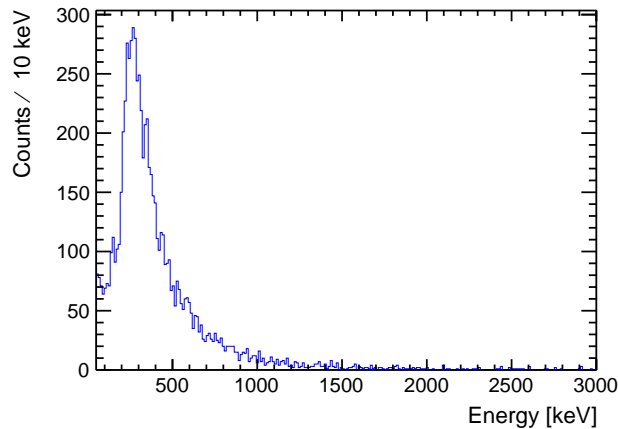


Figure 4.4.: Energy deposit of 270 GeV muons in Silicon Drift Detectors.

make a histogram  
really over whole  
range

keV. In all 6 SDDs combined there were 7896 hits in 7744 different events. This equates to a rate of 0.0224 Hz or 1 event about every 45 seconds. The energy

range of the SDDs is divided into a range of 1 keV - 30 keV and the energy  $> 30$  keV, as everything above this value is in the overflow bin of the ADC. Therefore it makes sense to calculate the rates for these 2 energy ranges. There are 338 hits in the lower energy range, meaning 14 hits per day in each SDD. In the higher energy range there are 7558 hits.

From the 7896 SDD events, 7859 events had an energy deposit of more than 100 keV in the inner and the outer scintillator layer. A signal in boths layers is the condition for a rejection and the threshold of 100 keV will be justified in chapter 5. This means, the background from cosmic rays can be rejected to  $\sim 99.5\%$ . A low energy spectrum of the SDDs with and without scintillator veto is shown in figure 4.5.

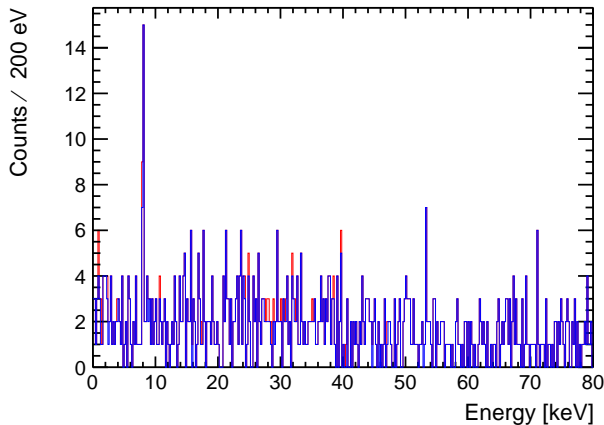


Figure 4.5.: Complete low energy spectrum of the SDDs induced by muons (red) and the part that is also seen by the scintillators (blue).

The underground laboratory LNGS lies at 3800 m water equivalent depth, where the cosmic muon flux is reduced to  $3.41 \times 10^{-4} \text{ m}^{-2} \text{ s}^{-1}$  [40]. Compared to  $1.67 \times 10^2 \text{ m}^{-2} \text{ s}^{-1}$  given in [38] for the surface of the earth, this is a reduction by a factor of  $2 \times 10^{-6}$ . The values for the event rates due to cosmic muons calculated in the previous section scale accordingly. The expected hit rate for each scintillator is then  $\sim 3.4 \times 10^{-6} \text{ Hz}$  or  $\sim 1$  event every 3 days and  $\sim 2$  events per day for all scintillators. The expected event rate for  $\sim 1$  event every 260 days for all 6 SDDs.

### 4.3. Gamma Ray Background

Energy spectrum in scintillators

Energy Spectrum of background

$6.3 \times 10^8$  into one half-sphere seems to be correct

The background consisting of  $\gamma$ -rays is the dominant background in the underground laboratory LNGS, as cosmic radiation is reduced by almost 6 orders of magnitude. The origin of the  $\gamma$  radiation are long-lived  $\gamma$ -emitting primordial isotopes. They are part of the rocks of the Gran Sasso mountains and the concrete used to stabilize the cavity. The dominant isotopes of this kind are  $^{238}\text{U}$ ,  $^{232}\text{Th}$  and  $^{40}\text{K}$  [41] and their decay products. For the simulation  $2.5 \times 10^9$   $\gamma$  photons were generated on a surface of  $0.945 \text{ m}^2$ , which completely enclosed the setup. The particles energy distribution follows the one reported in [41] in the dominant energy range from 40 - 500 keV, which was modeled by a Landau distribution with a mode at 120 keV and a sigma of 50 keV. The particles directions were randomized in the half sphere towards the setup. In [41] an integral flux of  $0.33 \text{ } \gamma \text{ cm}^{-2} \text{ s}^{-1} = 2.85 \times 10^8 \text{ } \gamma \text{ m}^{-2} \text{ day}^{-1}$  was reported, whereas in [42] a flux of  $6.3 \times 10^8 \text{ } \gamma \text{ m}^{-2} \text{ day}^{-1}$  was given. For now the data from [41] will be used and later the result of this assumption will be compared with the measured data. In this case the simulated  $2.5 \times 10^9$  particles correspond to a data taking time of 9.28 days.

The interaction of the photons with the scintillators almost exclusively takes place via inelastic Compton scattering, meaning the photons do not deposit the complete energy. The deposited energy can be as high as 500 keV. In the 9.28 days of the simulated data, there were 184,380 events with an energy deposit in the inner and outer scintillator layer larger than 100 keV. As the trigger condition is a signal in inner and outer layer, the trigger rate from these events is 0.23 Hz or  $\sim 1$  event every 4 seconds in all scintillators. The energy spectrum in the range from 1 keV - 30 keV deposited in the SDDs is shown in figure 4.6. In the figure the Cu K $\alpha$  and K $\beta$  lines are visible at 8 - 9 keV as well as the Zr K $\alpha$  and K $\beta$  lines at 16 - 18 keV. The Cu lines come from photons from the Cu target and the Zr lines come from photons from the Zr calibration foil. This foil is mounted in the setup for the possibility to conduct an energy calibration of the detectors with an X-ray tube. In the 9.28 days of simulated data, there were 57,617 events in all SDDs with an energy deposit  $> 1$  keV, corresponding to a rate of 0.07 Hz or  $\sim 1$  event every 14 seconds in all SDDs. From these events, 30,581 are in the range between 1 keV - 30 keV, corresponding to a rate of  $\sim 0.04$  Hz. Comparing these rates to the ones induced by cosmic muons at LNGS, it is obvious that  $\gamma$  radiation is the dominant source of background.

From the 57,617 events in all SDDs with an energy deposit  $> 1$  keV, 604 events have an energy deposit in the inner and outer scintillator layer and can therefore be rejected. The rejection ratio is therefore  $\sim 1\%$ . A plot of the full energy

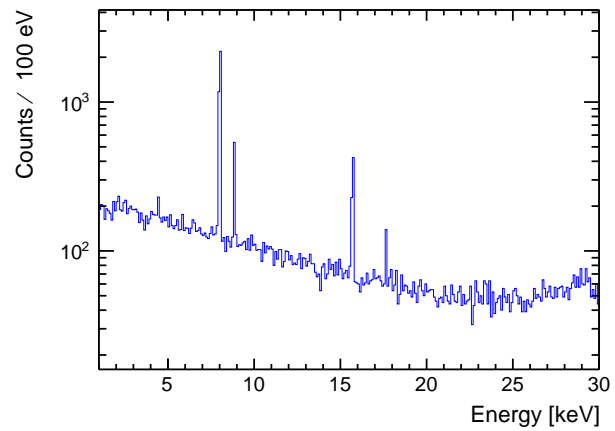


Figure 4.6.: Monte Carlo simulation of the energy spectrum induced by  $\gamma$  rays and detected by SDDs. Cu and Zr lines are visible at  $\sim 8$  keV and  $\sim 16$  keV respectively.

spectrum seen by the SDDs with the part that can be rejected is shown in figure 4.7.

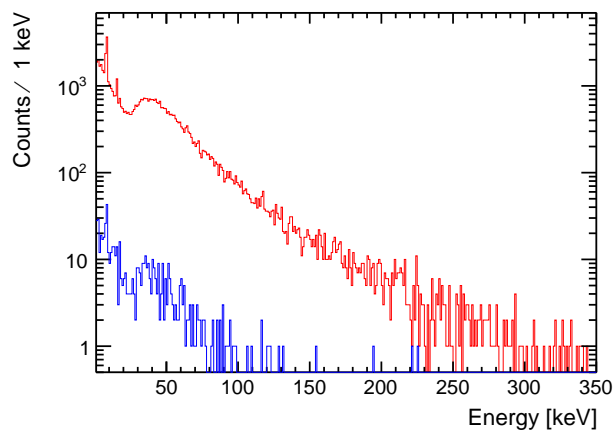


Figure 4.7.: The full energy spectrum introduced in the SDDs by  $\gamma$  radiation (red), with the part that can be rejected by scintillator veto (blue).

# 5. Test Measurements

scintillator + sipm detection ratio for cosmics (smi) and for 500 mev electrons (lnf test beam); background rejection at smi (tdc+qdc correlation) -> test of the functionality of the daq; sdd time resolution tests, sdd energy resolution determination (-> thereby also testing the cryogenics); tests with high current and water cooling; determination of the energy deposit threshold for the scintillators

time resolution sipms:  $\text{tr} \rightarrow \text{Draw}((\text{tdc}[14]-\text{tdc}[1])-(\text{tdc}[14]-\text{tdc}[7])) \text{ h}(800, -400, 400), \text{tdc}[1] > 0$  and  $\text{tdc}[7]$ )

## 5.1. Test Measurements at LNF

First measurements with the scintillators read out by SiPM were done at the Beam Test Factory (BTF) at Laboratori Nazionali di Frascati (LNF). This facility is connected to the linear accelerator of the DAΦNE collider and provides a 500 MeV electron or positron beam. The test setup is shown in figure 5.1, The scintillators

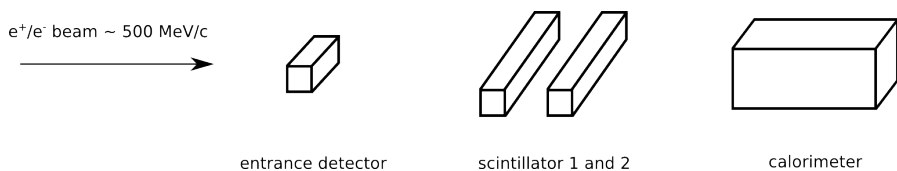


Figure 5.1.: The setup for testing the plastic scintillators with SiPM readout at the Beam Test Facility.

were the ones later on used in the VIP2 experiment, namely plastic scintillator bars of  $25 \text{ cm} \times 4 \text{ cm} \times 3.8 \text{ cm}$ . The trigger is defined as signal in the calorimeter AND a signal in the entrance detector, for which another scintillator was used. In case both of these detectors have a signal, both scintillators also need to have a signal because the triggering particle necessarily passes through them. The detection efficiency for any of the two scintillators is defined as the fraction of total triggers,

for which each scintillator produces a signal over threshold. Furthermore 3 different beam positions relative to the SiPM readout have been set, as shown in figure 5.2. The detection efficiency was larger than 98 % for all the beam hit position but

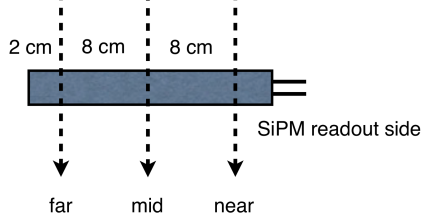


Figure 5.2.: 3 different beam positions for the tests of the scintillators at the Beam Test Factory.

no clear dependence on the hit position could be found. For each measurement the analog data from the SiPMs was converted to a digital signal in a QDC. The distribution of this signal in each case followed a Landau distribution. The most probable value of this distribution was dependent on the beam hit position and it was decreasing with increasing distance between the hit position in the readout. This means the scintillation light losses over the length of the scintillator have a measurable effect. Due to the 16 cm difference in beam hit position, the signal was decreased further away from the SiPM readout to 93 % and 87 % for the 2 scintillators respectively. The signals from the SiPMs were converted into time stamps by a TDC. By comparing these time stamps to a reference time stamp from the trigger, a time resolution of 2.6 ns (FWHM) could be estimated.

## 5.2. Test Measurements at SMI

smi data: 3 days and 19.5 hours

After first tests at LNF, the setup box as well as the scintillators and 2 SDD arrays which originally belonged to the SIDDHARTA experiment were transported to the Stefan Meyer Institute in Vienna in summer 2014. Tests were done with the SDDs in a smaller setup, but due to problems with Wi-Fi signals, which were probably picked up due to the similarity of Wi-Fi wavelength ( $\sim 12$  cm) and setup geometry, these tests were abandoned. Further tests were conducted with an adapted readout board in the final setup box, which was larger and therefore less likely to pick up Wi-Fi signals. The scintillators were wrapped in aluminum foil and black tape and 2 SiPMs were attached to a surface with optical glue and read out in series.

The functionality of each system of scintillator read out by 2 SiPMs was tested by connecting it the signals to an oscilloscope and checking the signals. The slow control was set up including the current supply, the temperature controller and the Pt-100 temperature sensors with their positions described in 3.4.2. The PID values of the LakeShore331 temperature controller were adjusted to ensure stable operation. The data acquisition system was set up and connected to the signals from the SDDs and the scintillators. The gain and shaping time of each SDD channel was adjusted in the CEAN 568B spectroscopy amplifier. After all these parts were tested individually, they were assembled and long term tests were conducted which will be described subsequently.

### 5.2.1. Water Cooling of Cu Target

One of the first tests done in order to ensure adequate cooling of the Cu target also in the case of a high current. The cooling of the target is done by water flowing through the cooling pad between the 2 copper target foils. The temperature was measured on each foil with a Pt-100 temperature sensor. 2 different measurements were done, with a high current once with and once without water cooling. The outcome is shown in figure 5.3.

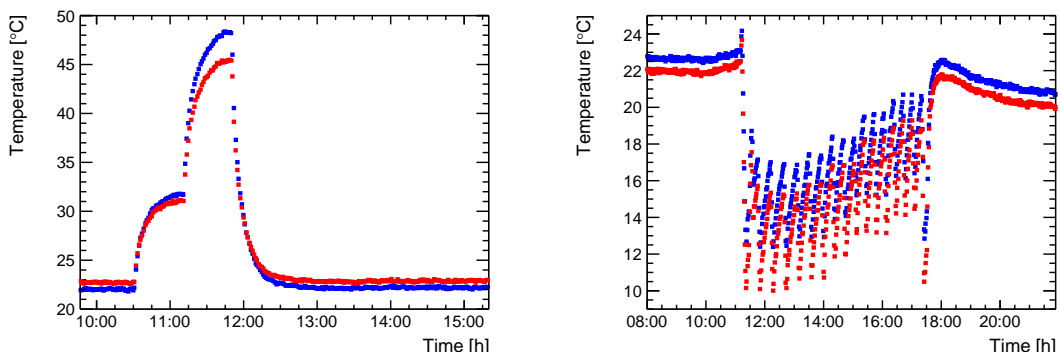


Figure 5.3.: The temperature of the 2 Cu target foils with a high current without water cooling (left) and with water cooling (right).

The left figure shows the temperatures without the water cooling with a current of 40 A (starting at  $\sim 10:30$ ) and a current of 80 A (starting at  $\sim 11:15$ ). The temperature rises to  $\sim 45$  °C, well above room temperature. As even higher current of 100 A is projected, it is not an option not to use water cooling. On the right picture the temperature of the Cu target with water cooling is shown. In this case the current was varied gradually from 80 A (starting at  $\sim 13:00$ ) to 180 A

(starting at  $\sim 16:00$ ). In this case the temperature can be stabilized below room temperature even for a current as high as 180 A. Consequently similar temperatures of the target can be achieved for data taking with and without current.

### 5.2.2. Argon Cooling of Silicon Drift Detectors

maybe add argon target + argon pressure correlation; tr->Draw("slow[3]:slow[15]", "text")  
which metal?

The argon cooling of the SDDs was tested in many the test runs at the Stefan Meyer Institute. The Pt-100 temperature sensors were mounted on the metal support structure of the SDDs, which is in thermal contact with the detectors. During these data taking periods, the temperature of the detectors could be kept constant at around  $-170$  °C, except for short periods of higher temperature, with a duration of a few minutes typically. The temperature for both SDD arrays during 1 day of data taking is shown in figure 5.4. As the scheduled operation temperature

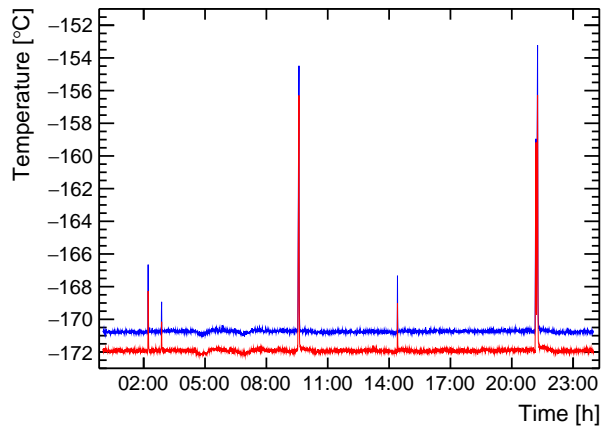


Figure 5.4.: Temperature of the 2 SDD arrays during 1 day of data taking at the Stefan Meyer Institute.

is 150 K [31] ( $\sim -120$  °C), which is still higher than during the periods with higher temperature, the performance characteristics of the detectors are not affected by these changes. But nevertheless this problem was solved in the measurement at the Gran Sasso National Laboratory (LNGS) by adding a bit more Argon to the cooling system, which ensured stable data taking conditions at a SDD temperature of around 100 K.

### 5.2.3. Scintillator Energy Deposition Trigger Threshold

To find out the minimum energy that needs to be deposited in the scintillators by ionizing radiation in order for the event to be detectable, we used a Caesium-137 <sup>1</sup> source shining directly into plastic scintillators used in the VIP2 experiment parallel to their length axis. A 2 mm aluminum plate was mounted between the source and the scintillator in order to shield the  $\beta$ -radiation from the source. The scintillators were read out by 2 serially connected SiPMs on the opposite side of the source. The pulse-height spectrum of the SiPMs was recorded with an oscilloscope. The setup was modeled in the Geant4 framework and the energy deposited in the scintillator was recorded. The deposited energy was smeared in the simulation by 10 % to account for the finite resolution of the detection system. The pulse-height spectrum from the oscilloscope and the MC-spectrum are shown in figure 5.5. The

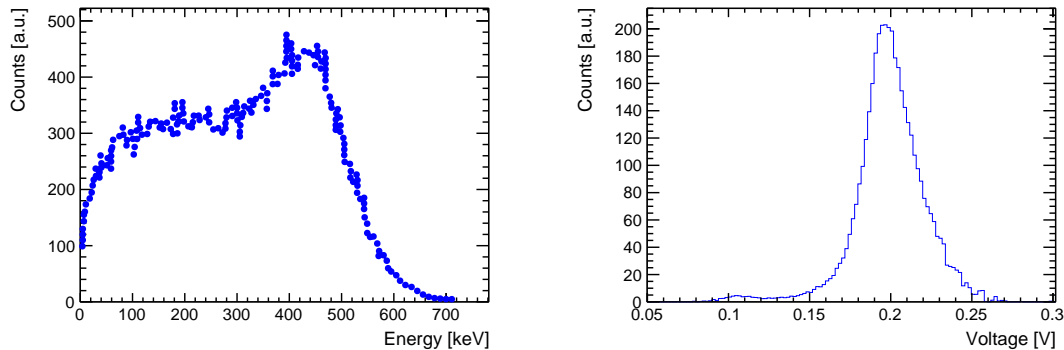


Figure 5.5.: The spectrum of energy from a Cs-137 source deposited in the scintillator from MC-simulations (left) and the pulse-height spectrum recorded with an oscilloscope (right).

pulse-height spectrum was recorded once with and once without the source. The subtracted spectrum was calculated in order to get the isolated spectrum from the source without events from external radiation. This subtracted spectrum is shown in the plot.

In the energy region of  $\sim 80$  keV -  $\sim 4$  MeV (which includes the photons from the Cs-137 source) the dominant energy-loss mechanism for photons in a plastic scintillator is the Compton effect [33]. Therefore not the whole energy of the photons is deposited in the detector. The falloff in the MC-spectrum corresponds

---

<sup>1</sup>Cs-137 decays to a metastable Barium-137 state via  $\beta$ -decay with a half-life of about 30 years. This state then decays into a stable state via emission of a 662 keV photon.

to the Compton edge <sup>2</sup>. The single Compton edge of 662 keV photons is at 478 keV, higher energies in the MC-spectrum come from Multi-Compton processes and from the smeared energy resolution.

The falloff in the pulse height spectrum at  $\sim 200$  mV corresponds to this Compton edge. The part below  $\sim 180$  mV is partly cut from the spectrum due to the trigger settings of the oscilloscope and does not have any physical meaning. From this measurement a relation between deposited energy and output pulse height of:

$$\frac{\text{Energy}}{\text{Pulse Height}} \approx \frac{500 \text{ keV}}{200 \text{ mV}} = 2.5 \frac{\text{keV}}{\text{mV}} \quad (5.1)$$

Furthermore the threshold settings in the experiment at LNGS were set to about 40 mV. They could not be set lower than this, as at lower thresholds the rate of dark counts rises and this needs to be avoided. With  $2.5 \frac{\text{keV}}{\text{mV}}$  a threshold of 40 mV corresponds to a deposited energy of 100 keV. This energy is used as a threshold for MC simulations, which were discussed in chapter 4. For the measurements at SMI the SiPM thresholds were set higher, as at this point the goal was to detect events induced by cosmic radiation, which have a typical energy deposit of a few MeV.

There are a few assumptions going into this calculation, as for example the linearity of the relation between deposited energy and output pulse height. Therefore the value of 100 keV energy deposition threshold at LNGS should be viewed as an estimation rather than a fixed value.

#### 5.2.4. SDD Energy Resolution

The following tests of the functionality of all parts are extracted from a data taking period from 23. October 2015 - 27. October 2017, corresponding to 4 days of data taking time. There was no current flowing through the copper target during this data taking period.

To achieve the optimal energy resolution, the voltage values for the photon entrance window ( $B_c$ ) and the separation mesh ( $B_f$ ) (see chapter 3.1) were adjusted, before this data taking period, starting from the values used in the SIDDHARTA setup for these SDD cells. The values used are summed up in tables 5.1 and 5.2.

---

<sup>2</sup>When a photon scatters on a charged particle, the energy it transfers to the charged particle depends on the angle between incoming and outgoing photon. The maximum energy is transferred when the photon changes direction by  $180^\circ$ . As a photon can not deposit more energy in a single process, this energy marks an “edge” in the detected spectrum.

Rx	R1	Bf (SDDs: 1,2,3)	Bf (SDDs: 4,5,6)
-250 V	-16 V	-137 V	-144 V

Table 5.1.: Voltages for outer and inner SDD rings as well as for the separation meshes of the 2 SDD arrays.

Bc1	Bc2	Bc3	Bc4	Bc5	Bc6
-134 V	-121 V	-143 V	-133 V	-137 V	-144 V

Table 5.2.: Voltages for the photon entrance windows for SDDs 1-6.

After optimizing the voltage settings, the energy resolution was determined from the data taken in the data taking period in October 2015. The results are shown in table 5.3.

	SDD 1	SDD 2	SDD 3	SDD 4	SDD 5	SDD 6
FWHM @ 6 keV	148 eV	150 eV	147 eV	147 eV	156 eV	158 eV

Table 5.3.: Energy resolution (FWHM) of the SDDs @ 6 keV.

The typical statistical error of the Full Width Half Maximum (FWHM) energy resolution is 1-2 eV for this amount of data for one SDD. These energy resolutions are close to the design resolution of 150 eV (FWHM) at 6 keV given in [31]. Furthermore an approximate Fano factor of 0.137 with a statistical error of 0.007 was found. The summed up energy spectrum is shown in figure 5.6.

The Mn K $\alpha$  and K $\beta$  lines (5.9 keV and 6.5 keV) from the Fe-55 source and the Ti K $\alpha$  and K $\beta$  lines (4.5 keV and 4.9 keV) from the Ti calibration foil are visible. The Mn and Ti K $\alpha$  lines are used to find the energy scale. Details to the calibration procedure will be given in chapter 6. Furthermore the Silicon K $\alpha$  escape peak <sup>3</sup> is visible 1.7 keV below its main peak at around 2.8 keV. The Cu K $\alpha$  line at 8 keV is caused by external radiation hitting the Cu parts and creating vacancies in the 1s shell which are subsequently filled by electrons from the 2s shell. As the thermal energy at room temperature ( $\sim$  25 meV) is orders of magnitude smaller than the gap between the 1s and the 2s shell ( $\sim$  8 keV), the creation of a vacancy in the 1s shell is reliant on an external energy source. All the expected peaks are therefore visible in the spectrum and the functionality of all 6 SDDs could be established.

---

<sup>3</sup>An Si K $\alpha$  photon escapes the detector. Its energy is therefore not converted into electron/hole pairs and is missing in the spectrum.

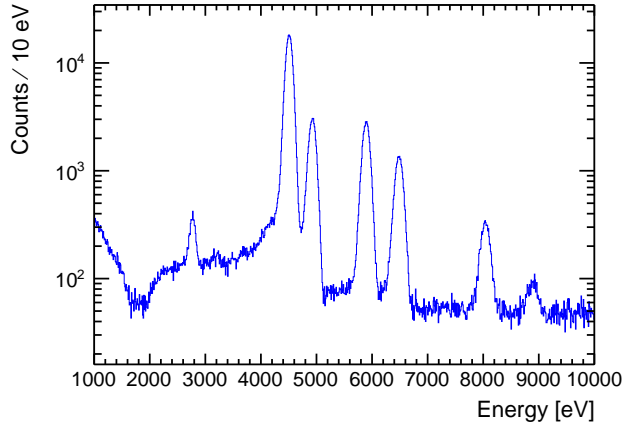


Figure 5.6.: Energy spectrum corresponding to 4 days of data taken at SMI.

### 5.2.5. SDD Time Resolution

For the measurement of the time resolution of the Silicon Drift Detectors, the arrival times of the digitized signals from the SDD “OR” and the SiPM “OR” at the TDC were compared. For details about the DAQ system see figure A.1 or section 3.4. As mentioned in 5.1, the time resolution of the scintillators read out by SiPMs is smaller than the one of the SDDs by around 2 orders of magnitude and is neglected here. The events in which both SDDs and scintillators give a signal are mainly caused by charged particles which first hit the scintillators and then either directly hit the SDDs or cause secondary radiation (e.g. bremsstrahlung in the scintillators), which in turn hits the SDDs. In either case the time difference of the actual hits of the radiation in scintillators and SDDs is also negligible compared to the time resolution of the SDDs. The difference in arrival times at the TDC between the 2 signals are shown in figure 5.7. The plot corresponds to all events with scintillator and SDD coincidence for the data taking period of 4 days at SMI. The time resolution was found to be around 380 ns (FWHM). This is in agreement with the specification of a time resolution  $\leq 1 \mu\text{s}$  given in [31]. Furthermore the mean delay of the arrival of the SDD signal is 290 ns.

### 5.2.6. Scintillator plus SiPM Time Resolution

For the mentioned 4 day data taking period, the difference in arrival times of signals from the adjoining “bottom inner” and “bottom outer” layer are shown in

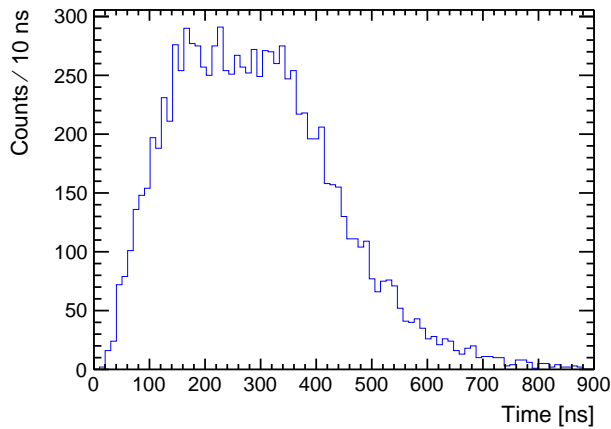


Figure 5.7.: Arrival time of the signal of Silicon Drift Detectors relative to the signal from the SiPMs corresponding to a time resolution of  $\sim 380$  ns (FWHM).

figure 5.8. The distribution of the difference of the arrival times can approximately

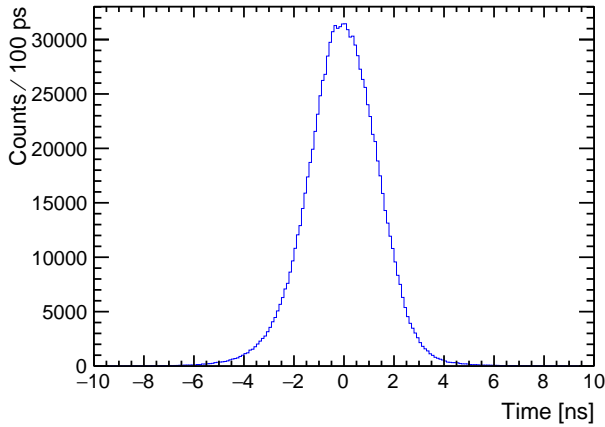


Figure 5.8.: Difference of arrival times of 2 different scintillator layers.

modeled by a gaussian distribution with a sigma of 1.38 ns or a FWHM of 3.25 ns. Assuming the time resolution is the same for both of these layers, this results in a sigma of 0.98 ns and a FWHM 2.3 ns for each layer and therefore also for each scintillator plus SiPM readout system.

### 5.2.7. Detection Efficiency of Cosmic Radiation and Active Shielding Test

0.993677 0.933823 0.93452

The data used for this test is again from the 4 day data taking period in October 2015 at SMI. The test was done in order to determine if particles from cosmic radiation going through the scintillators and potentially also through the SDDs were missed. The first step was to determine if any scintillator read out 2 SiPMs gave less signals than other scintillators. For this purpose the QDC spectra, which correspond to the charge deposited in the scintillator in each event, of each scintillator were investigated. One of these spectra with 2 different scales is shown in figure 5.9.

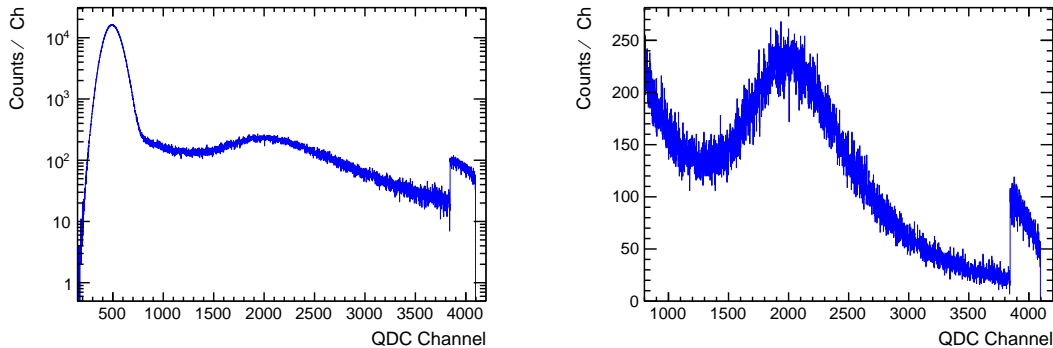


Figure 5.9.: Spectrum of charge collected by the QDC for 1 scinillator once in logarithmic scale (left) and once in linear scale (right).

The left figure shows a large peak on the left side. In these events the collected charge was low so it can be deduced that no ionizing radiation hit the scintillator. Starting from the about channel 800 there is a bump in the spectrum. For these events the collected charge was high and it can be said that there was probably ionizing radiation hitting this scintillator. To approximately determine the number of events in each scintillator, a threshold channel is introduced, above which all events where counted as signal events. This channel was determined as the  $3\sigma$  deviation from the mean value of the “No-Signal” gaussian distribution. In this case the threshold channel is 800. It is interesting to compare the collected charge distribution to the distribution of energy deposited in the scintillators by cosmic radiation, which is shown in figure 4.3. The peak in the QDC spectrum at channel 2000 corresponds to a deposited energy of around 8 MeV.

The distribution of the the counts determined in this way is shown in figure 5.10. The histogram is filled at positions corresponding to the positions of the scintillators in the setup, as they are shown in figure 3.5. One thing to note is that scintillators on the edge of the setup have less counts on average. This is due to the fact that for an event to be triggered, the inner and outer scintillator layer need to have a signal. Taking into account the angular distribution of cosmic radiation which is  $\propto \cos^2(\theta)$  [38], there is a chance of particles hitting for example the scintillator in column 1 and layer 5, but not hitting any other scintillator, not generating an event. This effect does not play a role for more central scintillators, like for example the one in column 3 and layer 4. For all these scintillators the number of hits is about 380.000 on average, which corresponds to a rate of 1.1 Hz in each scintillator. Comparing this rate to the 1.67 Hz extracted from [38], it is obvious that the system of scintillators does not detect a part of the cosmic ray spectrum. This might be due to the shielding of the aluminum enclosure and the multistory building above the setup. But from this plot one can say that all scintillators are working and giving signals.

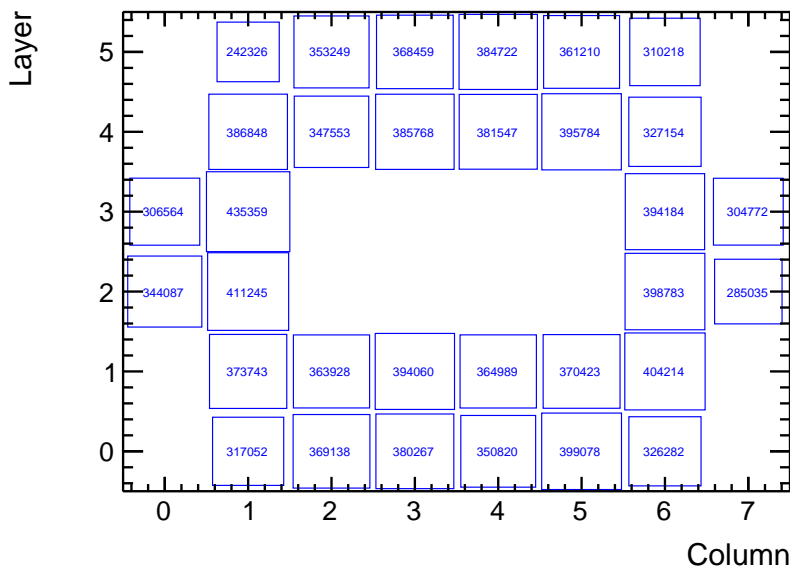


Figure 5.10.: The number of signals in each scintillator for a data taking period of 4 days.

To evaluate the detection efficiency for ionizing radiation in the energy region the scintillators should be sensible to, events were investigated in which at least 3 of the 4 scintillator layers with 6 scintillators had a signal. For these events the probability was measured that also the 4<sup>th</sup> layer had a signal. It turned out to be  $\sim$

90 %. A reason for this number not being higher might be that a part of the events are introduced by  $\gamma$  radiation, for which the detection efficiency is very low as was mentioned in 4.3. This radiation could introduce events in some scintillators, while in others it does not interact. Another factor might be differences in gain settings of the SiPMs and trigger threshold settings for the SiPM signals. These differences can again lead to radiation triggering signals in some scintillators, while in others it does not.

To ensure that the active shielding system is working as expected, it is interesting to look at hit patterns. For this purpose all events for which one specific scintillator has a signal are selected and then all events (from the previously selected events) every other scintillator has are counted. In figure 5.11 a hit pattern for the

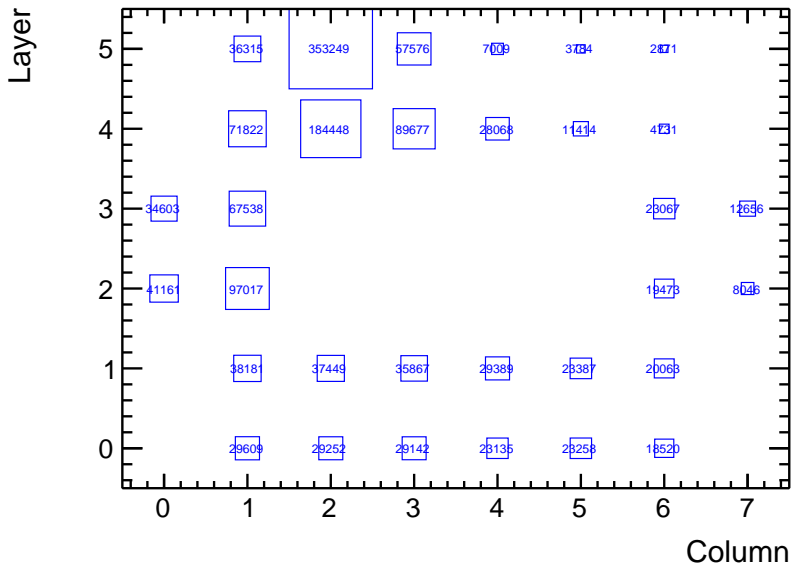


Figure 5.11.: Hit pattern for scintillator in column 2 and layer 5.

scintillator in column 2 and layer 5 is shown. It can be seen that for most events in this scintillator, the scintillator below also has an event, meaning most particles go through the setup almost vertically. Other scintillators not being directly below the specific scintillator get hit less often. The distribution resembles the  $\cos^2(\theta)$  distribution of cosmic radiation mentioned in [38]. As the hit patterns for all scintillators look as expected, it can be assumed that all scintillators are connected properly and working fine. Another test was done comparing the SDD spectrum of the events rejected by scintillator veto to the expected spectrum introduced in the SDDs by cosmic muons, which was already shown in figure 4.5. The expectation

was that these spectra should be similar as a big part of the signals introduced by cosmic muons is rejected as they also trigger a signal in the scintillators. These rejected signals should be similar to the the signals in the SDDs introduced by muons. The 2 spectra are shown in figure 5.12. The first thing to note is that the

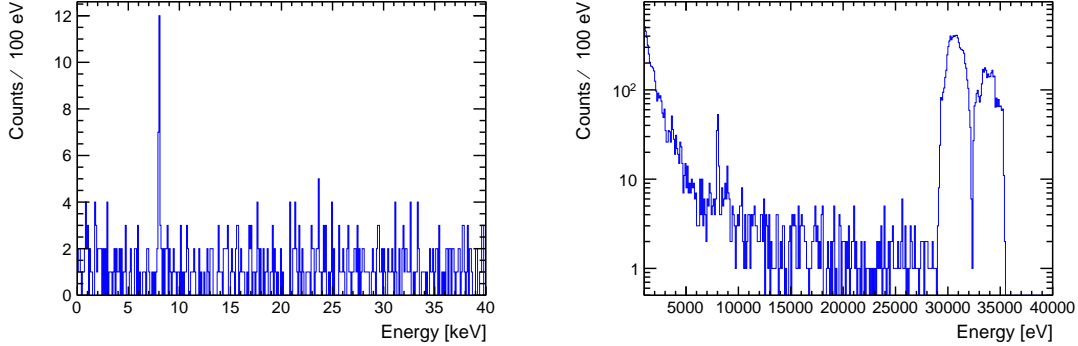


Figure 5.12.: The energy spectrum corresponding to 4 days of data introduced by cosmic radiation above ground from simulation (left) and measured (right).

peak at around 30 - 35 keV in the measured spectrum is artificial, as it is the upper end of the energy scale of the 6 SDDs. Every event with higher energy than that is filled in overflow bins. The overflow bins of the 6 SDDs correspond to slightly different energies, which makes the peak spread out over several keV. The second thing to note is that in the energy region from about 15 - 25 keV the 2 spectra are quite similar with about 1 count per 100 eV. In the energy range where the scintillator veto is crucial, the region of the forbidden Cu K $\alpha$  transition below 15 keV, there are more SDD hits rejected than there are predicted hits from cosmic radiation (consider the logarithmic scale on the right figure). This probably means that the scintillator veto can also reject at least a small part of the  $\gamma$  radiation which is present in the laboratory. Consequently the system is not only capable for what it was designed, namely detecting high energy ionizing radiation, but also detecting  $\gamma$  radiation.

Finally it is interesting to look at the amount of hits in the SDDs which are in coincidence with a scintillator signal. The complete spectrum together with the rejected events are shown in figure 5.13. It is obvious that only a small fraction of the SDD events can be rejected by scintillator veto. For example in the region of the the Cu lines from 7 - 10 keV a fraction of  $\sim 1\%$  of events is seen in the scintillators. This rejection ratio mean that the vast majority of counts in this energy region is caused by external photons, which can only be rejected to a

check if there is a  
change when a cut  
on the sdd multi-  
plicity is set.

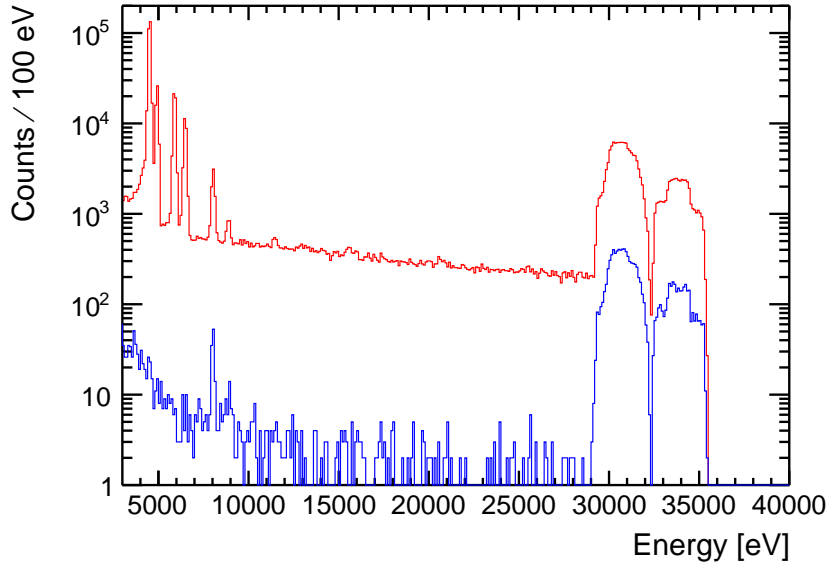


Figure 5.13.: The full energy spectrum corresponding to 4 days of data at SMI (red) and the part of the spectrum rejected by scintillator veto (blue).

small part. For this kind of radiation a rejection ratio of about 1 % was already reported as a result of simulations in section 4.3. For the part below 7 keV the Fe-55 source inside the setup contributes most of the counts, which can not be rejected. Therefore it does not make sense to calculate a rejection ratio for this energy region. The higher the energy the higher is the contribution of charged particles, with a high detection efficiency in the scintillators, to the SDD events. In the overflow bins of the SDDs, corresponding to an energy higher than around 30 keV, the rejection ratio is 6.5 %. The fact that the contribution of charged particles to the background is proportional to the energy can be seen comparing figures 4.4 and 4.7. While the peak contribution of charged particles is at around 300 keV, the contribution from external  $\gamma$  radiation is high from  $\sim 0 - 70$  keV or so, with a maximum on the low energy side.

The test of the active shielding system has shown that the detection of charged particles works with  $> 90$  % efficiency. All scintillators were found to work properly and contribute to the rejection of external radiation. But as the main background at SMI apparently comes from  $\gamma$  radiation, the background rejection ratio is as low as 1 % in the energy region of the forbidden transition. As all tests mentioned above gave the expected results it can be concluded that all detectors and parts of the data acquisition are working as expected. Crucial parameters of the experimental

setup like SDD scale linearity and peak position stability will be discussed in the the following chapter.



## 6. Data Taking at LNGS and Data Analysis

with data from lngs only, background comparison to smi; validation of the low rejection rate for gammas calculated first by simulations (200 kev energy threshold), problems with sipm noise, approximate cosmic rate at lngs -> 1 every 3 days approx reproduced; maybe stability of sdd temperature? -> with difference w/o current; slow control data: dependence of fwhm on: current, temperatures; crosstalk + data selection (where are high mul events coming from?); stability of rejection rate + background rate -> as rejection rate is not stable -> just show stable rate of counts in some energy region (-> mention the time with high rate); elements in spectrum?;

(synchronous) peak drift -> division of complete data set -> calibration of small files -> summation -> calibration, non-linearity!, desription of calibration function and calibration procedure;

lngs data: 198 days 7 hours = 81 days 10.5 hours with current and 116 days 20 hours no current; 81 days 9.5 hours no current small

calculation of counts in roi -> standard analysis, bayesian count based analysis, bayesian gaussian fit analysis; calculation of beta

After the exhaustive tests at the Stefan Meyer Institute, the setup of the VIP2 experiment was transported to the Laboratori Nazionali del Gran Sasso (LNGS) of INFN in November 2015. The laboratory is located beneath the Gran Sasso mountains in the italian Abruzzo region. The Apennine mountains above the laboratory provide a natural shielding from cosmic radiation corresponding to 3800 m water equivalent depth [40]. The flux of comsic muons in the underground is reduced compared to the flux above ground by about 6 orders of magnitude (see also chapter 4). The dominant background radiation for the experiment therefore does not come from cosmic radiation, but from  $\gamma$  radiation originating from radioactive isotopes like  $^{238}\text{U}$ ,  $^{232}\text{Th}$  or  $^{40}\text{K}$  and their decay products. These isotopes are part of the rocks and the concrete used to stabilize the cavity. The background reduc-

tion due to the shielding of the mountains is crucial for improving the final limit on the probability for the violation of the Pauli Exclusion Principle the experiment is able to set, as this limit is proportional to the square root of the background. A comparison of the spectra taken at Stefan Meyer Institute and at LNGS is shown in figure 6.1. The counts in the energy region of the forbidden transition at about

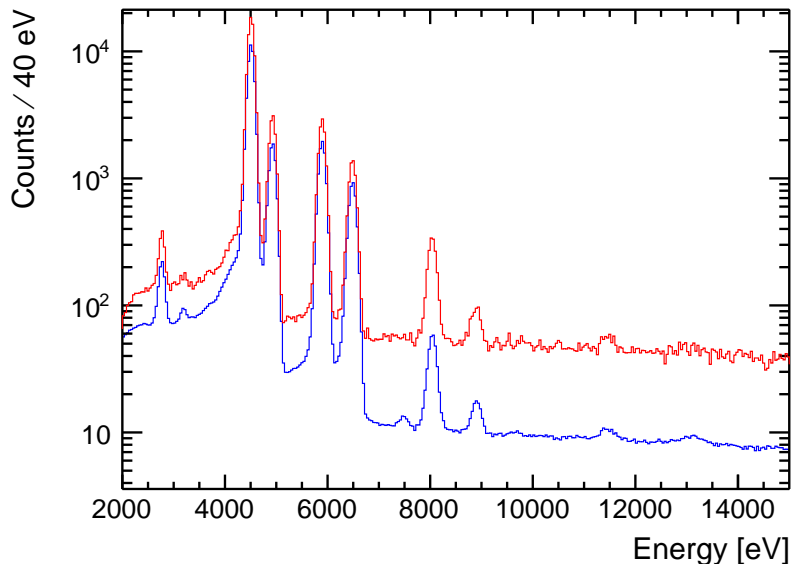


Figure 6.1.: The complete spectra from SMI (red) and LNGS (blue) both scaled to 1 day of data taking time.

7.7 keV are reduced by a factor of 5. In the region below 7 keV, the counts do not change drastically as in this energy region most of the events are caused by X-rays from the Fe-55 source and the titanium calibration foil. These counts are similar, as the source rate is the same at SMI and LNGS (apart from a slight decrease in the rate of the source due to its half-life of 2.7 years).

After some tests in November and a break over the Christmas holidays, the first data without current was taken in February 2016. After a period of further tests and maintenance and a data taking break in summer 2016, the first data with current was taken in October 2016. Data taking continued with various breaks for maintenance until November 2017 when problems with the argon cooling forced a stop. Parts of the VIP2 setup were then brought back to SMI for fixing these problems and to exchange the SDDs for ones with a larger active area and easier cooling (see for example [43]). The maintenance and experiment upgrade is still ongoing at the time this thesis is written (January 2018). Until the end of July

2017, a total of 116 days and 20 hours of data without current and 81 days and 10 hours of data with a current of 100 A have been taken at LNGS. After a break during summer 2017 which was used for maintenance, around 25 more days of data without current were taken until November 2017. Switching the current on during this period was not possible due to the problems with argon cooling. These 25 days are not included in this work.

## 6.1. Comparison of Data and Simulations

To check if the data corresponds to expectations, it is interesting to compare it to the simulations discussed in chapter 4. The measured counts above 7 keV together with the counts expected from simulations is shown in figure 6.2. The basis for the calculations was the  $\gamma$  spectrum reported in [42] with  $6.3 \times 10^8 \gamma \text{ m}^{-2} \text{ day}^{-1}$ . The good agreement between the measured data and the simulation based on this result favors it over the result reported in [41], where about half the  $\gamma$  flux was reported. This also shows that the by far largest contribution to the counts in the

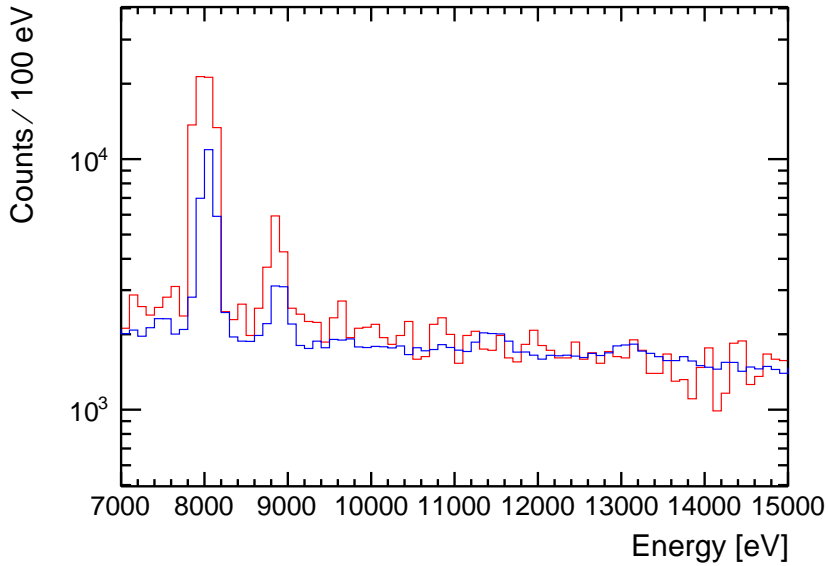


Figure 6.2.: The simulated spectrum introduced by  $\gamma$  radiation (red) scaled to the same data taking time (81 days 10 hours) as the data with current (blue).

region of the Pauli-forbidden transition at 7.7 keV is the  $\gamma$  radiation originating

from the surrounding rocks in the underground laboratory. No other sources of background need to be considered in order to reconstruct the observed spectrum.

The scintillator rejection rate of 1 % predicted by simulations can also be compared to the measured data. The spectra taken with and without current are shown in figure 6.3 together with the counts that can be rejected by scintillator veto. The

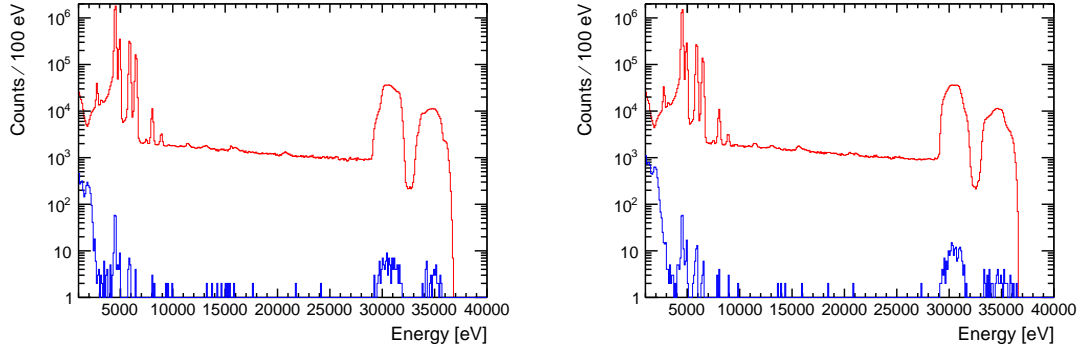


Figure 6.3.: The complete spectrum without current (left) and with current (right) in red taken at LNGS with the respective counts rejected by scintillator veto in blue.

rejection ratio for the counts above 7 keV is 0.02 % for the data with and without current. The 2 datasets were separated for this analysis in order to check for noise effects that might be introduced by the 100 A current in the data with current. But these effects were not observed here. Looking at the simulation data, a rejection rate of 0.02 % points to a minimum energy deposition of 200 keV in inner and outer scintillator layer to produce a veto signal. This value of 200 keV is double the value of 100 keV estimated for this threshold in chapter 5. But as this needs to be viewed as an estimation than a calculation, 200 keV can be accepted as the threshold value, despite this discrepancy. The trigger logic of inner AND outer scintillator layer instead of triggering on any scintillator signal was kept in order to avoid triggers from SiPM dark counts. As the trigger condition was an AND of the 2 layers, both layers would need to have a dark count in order to produce a dark count trigger. As these correlated dark counts are much more unlikely than single dark counts, they can be suppressed in this way.

The rate of high energy charged particles hitting the setup can be estimated from the spectra of scintillator signals recorded by the QDC. Events with high energy deposited in one scintillator can be attributed to these particles, as their energy deposition is typically higher than the one from  $\gamma$  radiation. This is difficult for 2 reasons: Firstly the count rate of high energy charged particles is very low,

on the order of a few counts per week per scintillator. Secondly the separation between events caused by  $\gamma$  radiation and charged particles is not unambiguous. Nevertheless a rate of 1 event per scintillator every 3 days can be estimated from the data. This is in good agreement with the rate given in [40] of  $3.41 \times 10^{-4} \text{ m}^{-2} \text{ s}^{-1}$ .

## 6.2. Effects of 100 A Current

fwhm w/wo current at some energy

It is interesting to look at effects of the 100 A current flowing through the Cu conductor on the measurements. One effect is the heat produced in the Cu conductor which then heats the SDDs, which are mounted about 0.5 cm away from the Cu strip. The temperature of the Cu strips is stabilized by a water cooling system and the temperature of the SDDs is kept constant by argon cooling (see also chapter 3). These cooling systems counteract the warming up of the detectors when the current is turned on. The measured SDD temperatures are shown in figure 6.4. The x-axis of this and similar upcoming plots spans a time from February 2016

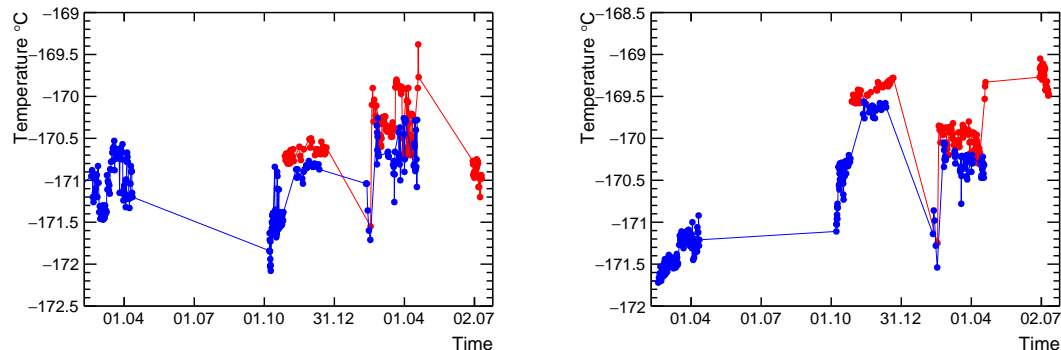


Figure 6.4.: Temperature measured on the metal frame of SDDs 1-3 (left) and on the metal frame of SDDs 4-6 (right). Data points with 100 A current are shown in red and data points without current are shown in blue. The x-axis spans a time from February 2016 until July 2017.

until July 2017. Each data point corresponds to a measurement at a randomly selected time for about each day of data taking time. This is again also valid for all similar upcoming plots. From the figures it can be seen that the 100 A current (red data points) only raises the temperature of the metal frame of the SDDs by about

0.2 - 0.4 °C compared to the measurements without current (blue data points). The temperature of the detectors themselves might be affected more than shown in the plots, but as there is no possibility to measure it directly it is impossible to be certain. Nevertheless it shows that the SDD environment can be stabilized at cryogenic temperature even with high currents. It is worth mentioning that the problems with suddenly rising temperature of the SDDs (see also chapter 5) were overcome during the measurements at LNGS by filling more argon gas into the system.

Another interesting effect of the 100 A current is that it influences the energy resolution of the silicon detectors. A plot of the energy resolution at 6 keV for different times of measurement with and without current is shown in figure 6.5. The resolution (FWHM) gets worse in times when the current is turned on by

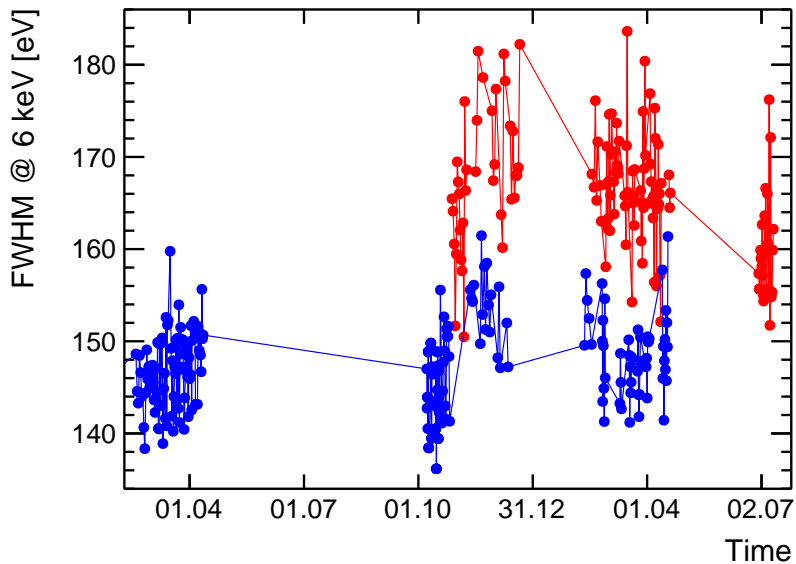


Figure 6.5.: Energy resolution at 6 keV for SDD 1 without current (blue) and with current (red).

about 20 eV. This effect might be caused by the temperature rise in the SDDs mentioned above. The dependence of energy resolution on temperature was for example reported in [32]. The change in temperature of the detectors would have to be higher than the 0.4 °C measured on their metal holder. The same effect of peak broadening due to a current was also reported in [18], where it was attributed to electronic noise introduced by the current. The energy resolution at 6 keV measured at LNGS with and without current for the complete data taking time

are shown in table 6.1 for each single SDD and for the spectrum resulting from the summation of all single SDDs. The energy resolution changes by about 10 eV

current	SDD 1	SDD 2	SDD 3	SDD 4	SDD 5	SDD 6	Sum
0 A	159 eV	151 eV	151 eV	149 eV	157 eV	163 eV	155 eV
100 A	177 eV	165 eV	166 eV	155 eV	160 eV	169 eV	165 eV

Table 6.1.: Energy resolution (FWHM) of the SDDs at 6 keV. Typical statistical uncertainty for the amount of data going into this calculation is 0.5 eV.

at 6 keV when turning on the current. The same effect of peak broadening due to the current also occurs at an energy of 8 keV where the Pauli-forbidden transition is expected.

### 6.3. Spectral Lines in the Energy Spectrum

The low background at LNGS gives the opportunity to study possible spectral lines from elements occurring in the equipment surrounding the detectors. Conclusions from this analysis might be used to improve future MC simulations of the setup. The complete energy spectrum taken at LNGS corresponding to about 198 days of data is shown in figure 6.6. The most prominent peaks are the Cu K $\alpha$  and Cu

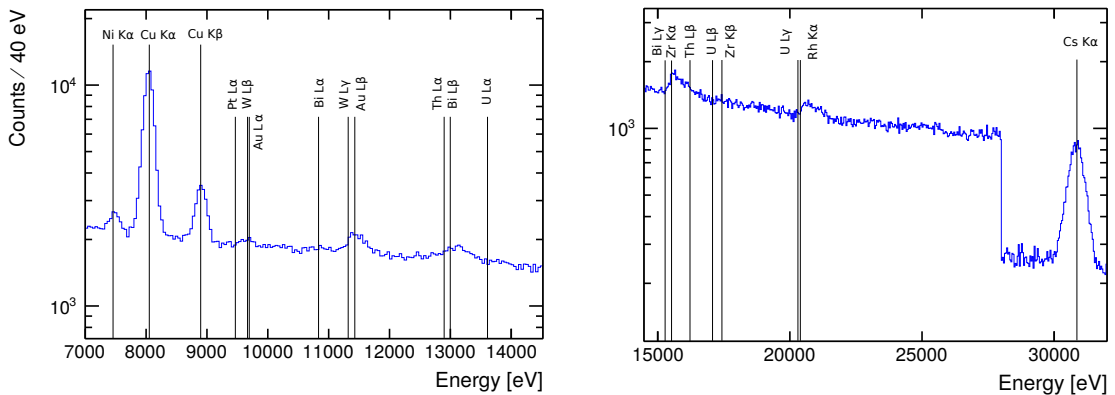


Figure 6.6.: Energy spectrum corresponding to 198 days of data taken at LNGS with candidates for spectral lines. The drop at 28 keV is artificial as above this energy, only 2 SDDs can be used, as the others are in overflow.

K $\beta$  peaks. The corresponding photons originate from the Cu conductor next to

the SDDs. Another peak of certain origin is the Ni K $\alpha$  peak at 7.5 keV. Nickel is for example used in stainless steel, from which the tubes of the argon cooling system and other parts of the setup are made. The Zirconium spectral lines come from a 15  $\mu\text{m}$  thick Zirconium foil mounted above the SDDs for initially planned calibration with an X-ray tube. The anode of this tube is made out of tungsten (W), from which the W L-lines might be coming from. Several other lines are drawn in the figure, which were suggested in [6]. As the 2 sources of calibration are Ti K $\alpha$  and Mn K $\alpha$  at 4.5 keV and 5.9 keV respectively, the energy calibration has a higher uncertainty for higher energies. This effect might limit the possibility to accurately determine the spectral lines with higher energy.

## 6.4. Data Selection

The selection of correct events is important in the VIP2 experiment. First SDD events were discarded which occurred in coincidence with an active veto signal. This was already discussed in chapter 6.1 for example.

Furthermore events were neglected which occurred in a time of a higher than normal background rate. Excluding any possible source of background, which causes events in the energy region of the forbidden Cu K $\alpha$  transition, is important as it makes finding possible candidate events from this transition more difficult. Figure

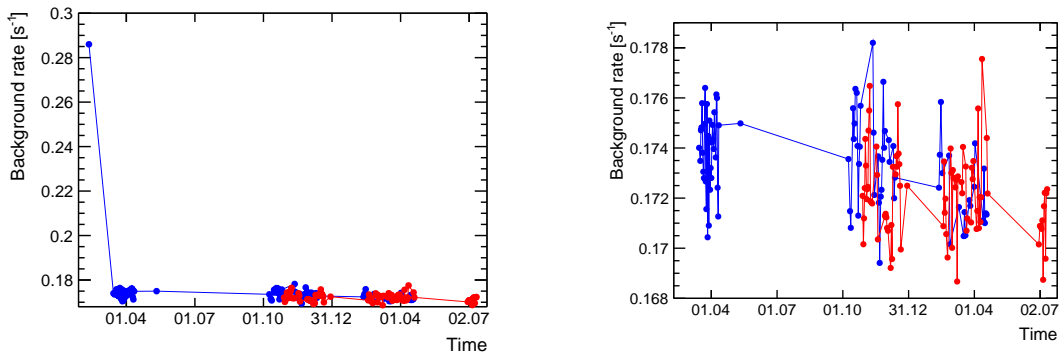


Figure 6.7.: The rate of events with an energy deposit larger than 7 keV for the complete dataset (left) and for the cleaned dataset (right). Each dot corresponds to 1 day of data.

6.7 shows the rate of events with an energy deposit above 7 keV in any SDD. The rate of events with an energy lower than that is dominated by events caused by

the Fe-55 source. The left picture shows the complete dataset. It shows a period of higher event rate by a factor of about 2 in the time around the 11. February 2016. The reason for this increase is not yet clear. These data were left out in the data analysis. The same event rate without these data is shown in the right picture of figure 6.7. The rate is stable throughout the whole period, which was then used for the analysis. It is interesting to look at the rate of events with an energy smaller than 7 keV, which are caused by the Fe-55 source mainly. Due to

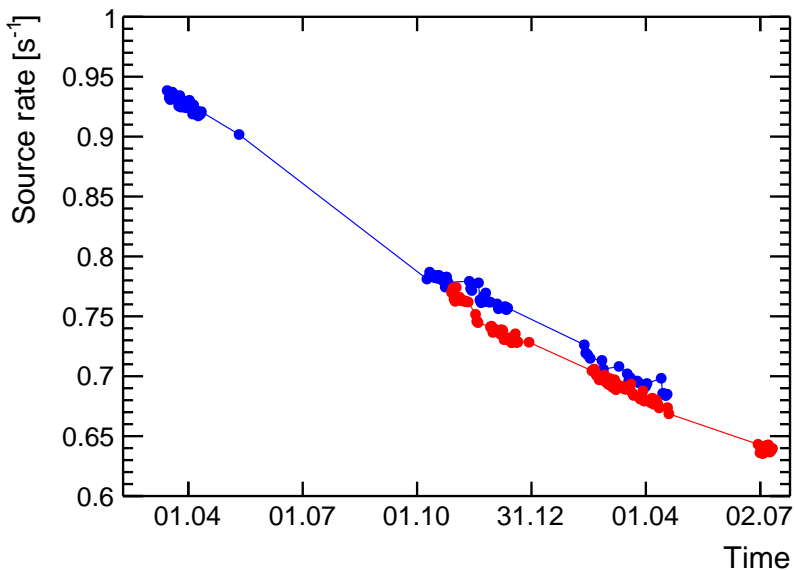


Figure 6.8.: The rate of counts caused by the Fe-55 source for the data with current (rate) and without current (blue). It is decreasing due to the half-life of Fe-55 of 2.7 years.

its half-life, events from the source decrease by a factor of 0.68 in the course of the data taking of 1 year and 5 months.

Events in the SDDs originating from a Pauli-forbidden transition are expected to hit only 1 SDD as only 1 photon is produced in the course of this process. Therefore all events with a multiplicity larger than 1 can be excluded when looking for those photons. The distribution of SDD hit multiplicity is shown in figure 6.9. The vast majority of events has an ADC multiplicity of 1, from which in turn the vast majority comes from the Fe-55 source. Additionally there are events caused by the environmental  $\gamma$  radiation and possibly events from non-Paulian transitions in the spectrum with 100 A current. All these are the ones that are used for the analysis. Events with SDD multiplicity 2-5 are caused by high energy  $\gamma$  radiation

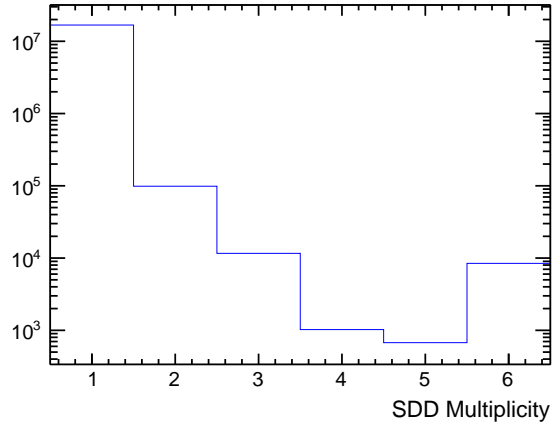


Figure 6.9.: Distribution of SDD hit multiplicity for the complete dataset taken at LNGS.

causing hits in several SDDs for example by generating multiple secondary photons. Another possibility of signals in 2 SDDs is a hit of any energy on the border of 1 SDD, where a part of the generated charge is transferred to the neighboring SDD. That events of this kind exist can be seen for example in figure 6.10. Here the charge generated by a photon either directly from the Fe-55 source or the Ti foil is split and drifts to the anodes of 2 neighboring SDDs. The energy equivalent to the total deposited charge equals the energy of one of the calibration lines. Consequently these lines run diagonally through the figure. Low energy parts are cut from the figure to enhance visibility. The vast majority of events with SDD multiplicity 6 are caused by noise. This can be said with certainty as their rate is fluctuating with time. It is also dependent on parameters it should not be connected with, like the SiPM trigger rate.

## 6.5. Energy Calibration

As the goal of the VIP2 experiment is to count events in the energy region of the Pauli-forbidden Cu K $\alpha$  transition, the determination of the energy of each SDD hit is of utmost importance. Assigning for example an energy of 7.7 keV to an event coming from a photon from a normal Cu K $\alpha$  transition at 8.05 keV changes the outcome of the experiment and has to be avoided. Furthermore the energy resolution should be kept as small as possible close to the intrinsic energy resolution of the detectors, in order to avoid events in the tail of the Cu K $\alpha$  line in

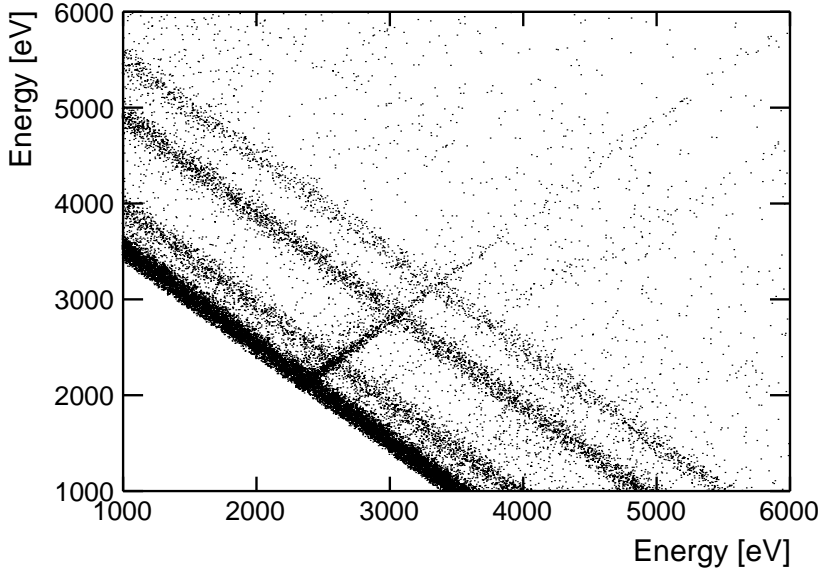


Figure 6.10.: Energy correlation between 2 neighboring SDDs. The Ti and Mn lines are visible on lines with a constant sum of energy due to cross talk between adjoining detectors.

the energy region of the Pauli-forbidden transition. A drift of the peak position is one of the effects that leads to a deterioration of the energy resolution and needs to be avoided.

An energy calibration of the detector is the conversion from the primary spectrum in ADC channels into energy in electronvolt. For this purpose the position of the Mn K $\alpha$  and Ti K $\alpha$  peak are determined in the primary spectrum. As the energies of these peaks are known, a linear relation between ADC channel and energy can be calculated. The ADC channel of every event is then scaled according to this linear relation into an energy. To determine the position of the peaks as precisely as possible, the complete spectrum is fit taking into account all features of a real detector. This fit function will now be discussed. In the fitting procedure, the relation for the energy resolution which is only dependent on fano and constant noise is assumed (see also chapter 3.1):

$$\sigma(E) = \omega \sqrt{W^2 + \frac{FE}{\omega}} \quad (6.1)$$

In equation 6.1,  $\omega$  is the energy needed to create an electron hole pair in silicon, which is 3.81 eV at 77 K [33].  $W$  denotes the contribution to noise independent

from energy and  $F$  is the Fano factor.

Photons from a monoenergetic source cause a complex spectrum in a real detector. For silicon detectors they were described for example in [44] and [45]. The main feature is the *gaussian peak*, corresponding to the case in which all electrons that are produced by the incident photon are collected at the anode. The width of this gaussian is determined by the intrinsic detector resolution and the natural line width. The natural line shape is a Lorentzian with a width of typically a few eV FWHM [46]. The intrinsic detector resolution gives rise to a gaussian line shape with a width of about 150 eV FWHM in our case. The real line shape is then a convolution of these 2 shapes, which would be a Voigt function. As the intrinsic detector resolution is by far larger than the natural line width, the latter contribution is small and the shape can be approximated by a gaussian function. On the low energy side of the main gaussian peak, there is a structure in the spectrum which is caused by incomplete charge collection. The effects contributing to these structures are summed up in [44]. Qualitatively they can be described by an exponential *tail* energetically right below the main peak and a *shelf* extending from the main peak to 0 energy. A *truncated shelf* extending from the energy of the main peak to smaller energy has also been described, but it was not used here. Furthermore a photon from a Si K $\alpha$  transition has a high chance of escaping the detector. These photons can originate from the photoeffect of the primary photon. These events are then seen as a so-called *escape peak* 1.74 keV (Si K $\alpha$  energy) below the main peak. *Pile-Up* effects do not play a role as the event rate is as low as about 1-3 Hz at LNGS. The mathematical structure of all the mentioned components is shown in equations 6.2 - 6.5 and is similar to the one used in [45]. The number  $i$  denotes the number of the ADC channel.

$$\text{Gaussian peak } (i) = \frac{\text{Gain}}{\sigma} \times \exp\left(-\frac{(i - i_0)^2}{2 \times \sigma^2}\right) \quad (6.2)$$

$$\text{Tail } (i) = \text{Gain} \times tR \times tN \times \exp\left(\frac{i - (i_0 + tSh)}{\sigma_{tail} * tSl}\right) \times \text{erf}\left(\frac{1}{\sqrt{2} * tSl} + \frac{i - (i_0 - tSh)}{\sqrt{2} * \sigma_{tail}}\right) \quad (6.3)$$

$$\text{Escape } (i) = \text{Gain} \times eR \times \frac{1}{\sigma_E} \times \exp\left(-\frac{(i - (i_0 - SiK\alpha))^2}{2 \times \sigma_{escape}^2}\right) \quad (6.4)$$

$$\text{Shelf } (i) = \text{Gain} \times sR \times \frac{1}{2} \times \text{erf}\left(\frac{i - i_0}{\sqrt{2} \times \sigma}\right) \quad (6.5)$$

Here  $\text{erf}()$  denotes the error function. A schematic drawing of the structure of a monoenergetic peak in the detected spectrum is shown in figure 6.11. The parameters used in equations 6.2 - 6.5 are described in detail in table 6.2. The parameters are fit for the Mn K $\alpha_1$ , K $\alpha_2$ , K $\beta$  and for the Ti K $\alpha_1$ , K $\alpha_2$ , K $\beta$  lines.

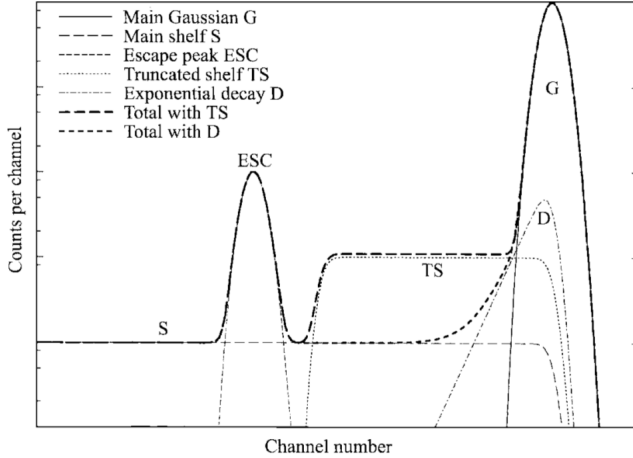


Figure 6.11.: Detected spectrum from monoenergetic incident radiation with a structure described in the text [44].

The gain ratio of the  $K\alpha_2$  to  $K\alpha_1$  lines is fixed to 0.51 for Mn and to 0.5 for Ti. The sum of all the functions is obviously fit to the data. The positions of the Mn  $K\alpha_1$  and Ti  $K\alpha_1$  is used to find the linear relation between ADC channels and energy. When the amount of data is high enough, the Cu  $K\alpha_1$ ,  $K\alpha_2$  and  $K\beta$  lines are fit in a similar way. Other lines shown in figure 6.6 are not fit due to too low statistics. A typical fit with residuals is shown in figure 6.12. The reduced  $\chi^2$  of the shown fit is 1.3. From the fit the linear relation between energy and ADC channel can be derived. It is shown in figure 6.13.

## 6.6. Peak Stability and Data Splitting

The fitting procedure described in the chapter 6.5 can be used to determine the stability of the peak positions for the Mn and Ti peaks. The data taken at LNGS was analysed in this way. The result for 1 SDD is shown in figure 6.14, where each data point represents about 1 day of data. The peak position changes by about 20 ADC channels in the course of the data taking. This is a typical value similar for all 6 SDDs. As 1 ADC channel corresponds to about 9 eV in the final energy spectrum, the peak position changes by about 180 eV. In the case of the SDD for which the peak position is shown in the figure (SDD 3), the energy resolution at 6 keV would change from 151 eV for a small data set to 179 eV for the whole data taking period. As the energy resolution needs to be kept as small as possible in order to determine possible events in the energy region of the Pauli-forbidden

Parameter Name	Parameter Description	Fit Parameter
Gain	Gain of the main gaussian peak	Yes
$\sigma$	Detector energy resolution at the energy of the gaussian peak	calculated from fano and constant noise
$\sigma_{tail}$	Detector energy resolution at the energy of the peak of the exponential tail	calculated from fano and constant noise
$\sigma_{escape}$	Detector energy resolution at the energy of the escape peak	calculated from fano and constant noise
$i_0$	ADC channel of the main peak	Yes
tR	Ratio of the exponential tail to the main peak	Yes
tN	Norm of the exponential tail	No
tSh	Shift of the exponential tail to the low energy side	Yes
tSl	Slope of the exponential tail	Yes
eR	Ratio of escape peak to the main peak	Yes
SiK $\alpha$	Energy of the Si K $\alpha$ transition (1.74 keV)	No
sR	Ratio of the shelf to the main peak	Yes

Table 6.2.: Parameters going into the fit of the signal produced by monoenergetic radiation.

transition as accurately as possible, the data needs to be divided into subsets for calibration. The strategy for determining the energy of each event as well as possible is as follows:

- Find an data taking time for which the energy resolution is as small as possible and divide the whole data into subsets with this length.
- Conduct the energy calibration with these subsets and calculate the energy for each event.
- Sum up the energy of all events in all subsets, instead of summing up the ADC channels.

This approach avoids the unwanted effect of peak broadening due to the drift of the energy spectrum with time.

Finding the optimal time for the subsets of data means to minimize the energy resolution at about 8 keV, where the non-Paulian transition is expected. There

are 2 effects that need to be considered: Firstly the intrinsic energy resolution of the detector together with the drift of the energy scale with time gives a large contribution to the detector resolution. This contribution can be estimated with formula 6.1 and the measured resolutions from the Ti and Mn lines. This effect will contribute less when the time of the data subset is low, as the effect of the peak drift is then minimized. This can be seen from the right image in figure 6.15. The second contribution to the uncertainty in the determination of energy of an event around 8 keV comes from the statistical uncertainty of the peak position of the Ti K $\alpha_1$  and Mn  $\alpha_1$  calibration lines given by the fit. Taking into account the relation between ADC channels and energy as well as these statistical errors, the energy uncertainty at 8 keV can be calculated with error propagation. This contribution to the uncertainty increases with decreasing data taking time, as the statistical error of the calibration lines increases in this case. It is shown in the left image of figure 6.15. The numbers in the figure correspond to an average over all 6 SDDs and were calculated from a dataset of 30 days from LNGS without current, which was divided into subsets of 0.1, 0.25, 0.5, 1, 2 and 4 days. The above mentioned uncertainties were calculated for every subset and averaged. The Cu K $\alpha$  line itself can not be used for calibration due to its low event rate.

The variances of the 2 contributions can be added as:

$$\sigma_{tot} = \sqrt{\sigma_{det}^2 + \sigma_{stat}^2} \quad (6.6)$$

and the result is shown in figure 6.16. The results for all 6 SDDs have been averaged for this figure. The minimum energy resolution was found for a data taking time of 0.25 days or 6 hours. Therefore the data taken at LNGS was divided into parts with 6 hours each. As an interrupt of continuous data taking caused a mandatory stop for the current part, some parts had to be longer. For example a continuous data taking period of 14 hours was divided into 1 part with 6 hours and another one with 8 hours. In this manner 198 days and 7 hours of data were divided into 618 parts. For each of them each of the 6 SDDs was calibrated separately and the energy of each event was added to 1 final energy spectrum.

## 6.7. Scale Linearity and 2<sup>nd</sup> Order Correction

With the Ti and Mn K $\alpha$  lines as 2 sources of calibration it is not possible to determine if the relation between ADC channel and energy is linear over the whole spectral range. T

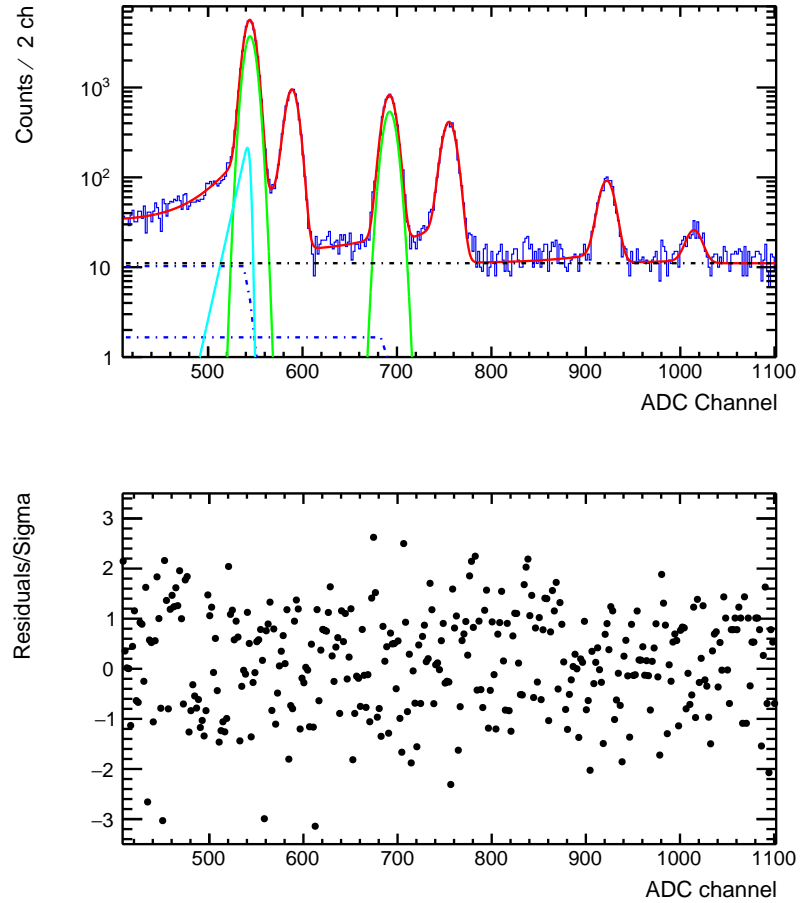


Figure 6.12.: Fit of data taken at SMI (blue) with the complete fit function (red). Some of the constituents of the fit function are shown like Ti and Mn K $\alpha_1$  peaks (green), constant background (black, dashed), Ti K $\alpha_1$  exponential tail (cyan) and the shelf functions of Ti and Mn K $\alpha_1$  (blue, dashed). Residuals are shown below.

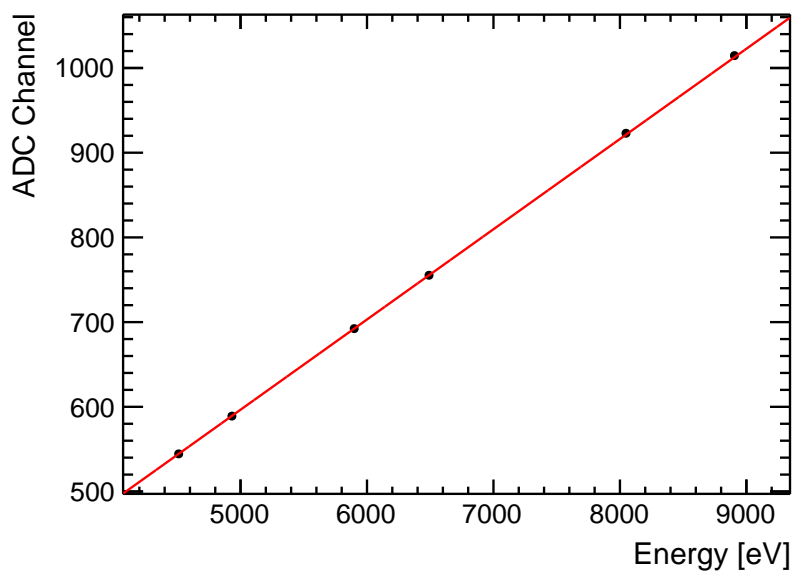


Figure 6.13.: The relation between ADC channel and energy for 1 SDD derived from Ti K $\alpha_1$  and Mn K $\alpha_1$  as 2 sources of calibration. Ti K $\beta$ , Mn K $\beta$  as well as Cu K $\alpha_1$  and K $\beta$  lines are also shown.

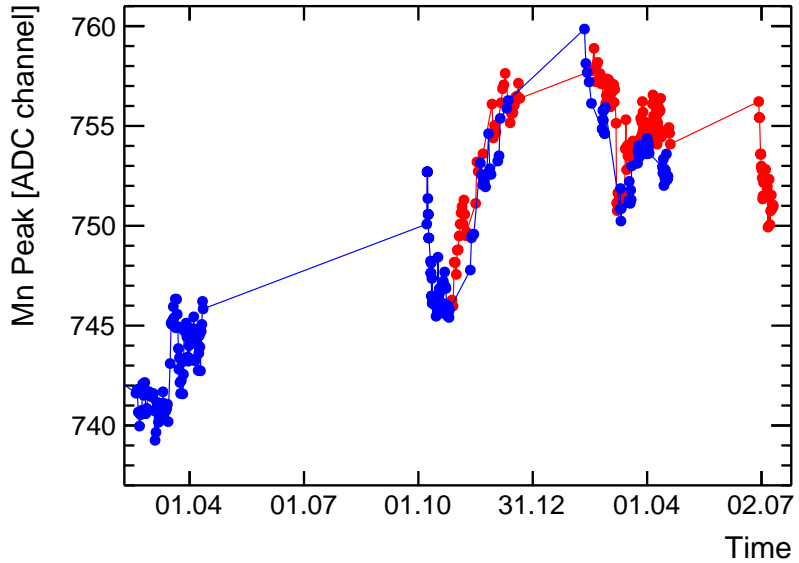


Figure 6.14.: The position of the Mn  $K\alpha_1$  peak for 1 SDD during the data taking at LNGS without current (blue) and with current (red). Typical statistical error is 1 ADC channel.

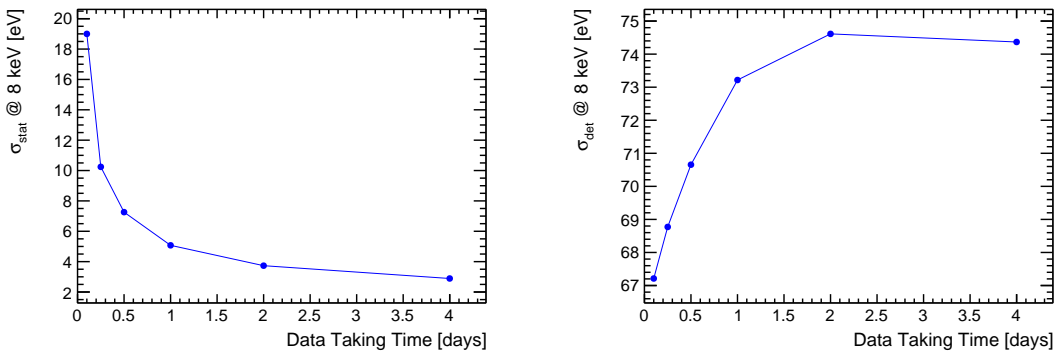


Figure 6.15.: Energy determination uncertainty at 8 keV due to statistical error of the position of the calibration lines as a function of data taking time (left). Energy resolution at 8 keV taking peak drift effects into account (right).

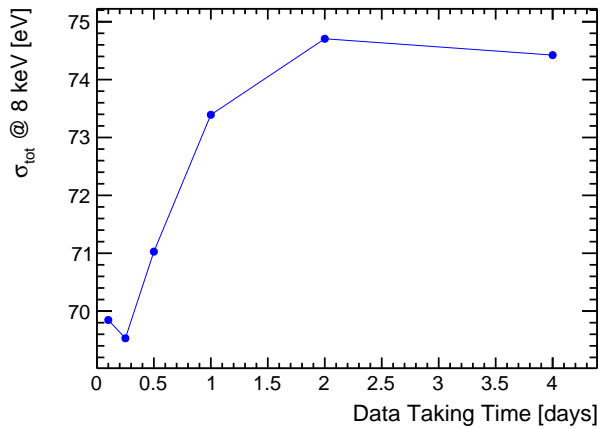


Figure 6.16.: The total uncertainty in the energy determination at 8 keV as a function of the data taking time.

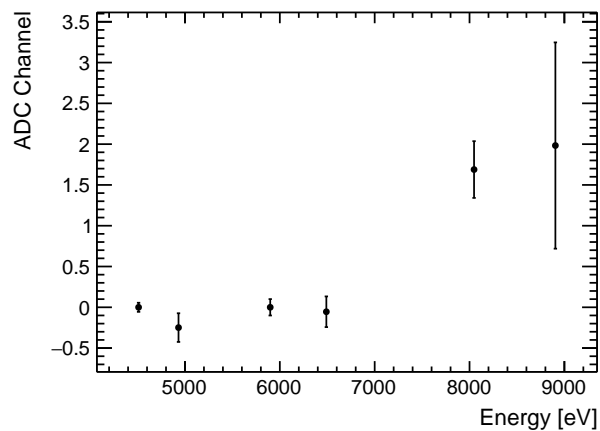


Figure 6.17.: bla.



## 7. Conclusion

sum up and conclude



# Bibliography

- [1] M. Goldhaber and Gertrude Scharff-Goldhaber. Identification of Beta-Rays with Atomic Electrons. *Physical Review*, 73(12):1472–1473, jun 1948.
- [2] Erik Ramberg and George A Snow. Experimental limit on a small violation of the Pauli principle. *Physics Letters B*, 238(2):438–441, 1990.
- [3] C Curceanu, S Bartalucci, A Bassi, S Bertolucci, M Bragadireanu, M Cargnelli, A Clozza, S Di Matteo, S Donadi, J-P Egger, C Guaraldo, M Iliescu, T Ishiwatari, M Laubenstein, J Marton, E Milotti, D Pietreanu, M Poli Lener, T Ponta, A Rizzo, A Romero Vidal, A Scordo, D L Sirghi, F Sirghi, L Sperandio, O Vazquez Doce, E Widmann, and J Zmeskal. Experimental tests of Quantum Mechanics: from Pauli Exclusion Principle Violation to spontaneous collapse models. *Journal of Physics: Conference Series*, 361:012006, 2012.
- [4] C. Curceanu, S. Bartalucci, S. Bertolucci, M. Bragadireanu, M. Cargnelli, S. Di Matteo, J. P. Egger, C. Guaraldo, M. Iliescu, T. Ishiwatari, M. Laubenstein, J. Marton, E. Milotti, D. Pietreanu, T. Ponta, A. Rizzo, A. Romero Vidal, A. Scordo, D. L. Sirghi, F. Sirghi, L. Sperandio, O. Vazquez Doce, E. Widmann, and J. Zmeskal. Experimental tests of quantum mechanics: Pauli Exclusion Principle Violation (the VIP experiment) and future perspectives. *Journal of Physics: Conference Series*, 306(1):012036, 2011.
- [5] W. Pauli. Nobel Prize lecture: Exclusion principle and quantum mechanics, 1946.
- [6] L. Sperandio. *New experimental limit on the Pauli Exclusion Principle violation by electrons from the VIP experiment*. PhD thesis, 2008.
- [7] A M L Messiah and O W Greenberg. Symmetrization Postulate and Its Experimental Foundation. *Physical Review*, 136(1B):B248—B267, 1964.
- [8] I. G. Kaplan. The Pauli Exclusion Principle. Can It Be Proved? *Foundations*

*of Physics*, 43(10):1233–1251, 2013.

- [9] W Pauli. The Connection Between Spin and Statistics. *Phys. Rev.*, 58(8):716–722, 1940.
- [10] J. Schwinger. Spin, Statistics and the TCP Theorem. *Proceedings of the National Academy of Sciences of the United States of America*, 44(2):223–228, 1958.
- [11] G. Luders and B. Zumino. Connection between Spin and Statistics. *Physical Review*, 110(6):1450–1453, 1958.
- [12] A. Stern. Anyons and the quantum Hall effect— A pedagogical review. *Annals of Physics*, 323:204–249, 2008.
- [13] H. S. Green. A generalized method of field quantization. *Physical Review*, 90(2):270–273, 1953.
- [14] O. W. Greenberg. Theories of violation of statistics. *AIP Conference Proceedings*, 545(1):113–127, 2000.
- [15] A.Yu. Ignatiev and V.A. Kuzmin. IS SMALL VIOLATION OF THE PAULI PRINCIPLE POSSIBLE? *International Centre for theoretical physics (Preprint)*, 87(13), 1987.
- [16] A.B. Govorkov. Can the Pauli principle be deduced with local quantum field theory? *Physics Letters A*, 137(1-2):7–10, may 1989.
- [17] O. W. Greenberg. Particles with small violations of Fermi or Bose statistics. *Physical Review D*, 43(12):4111–4120, 1991.
- [18] S R Elliott, B H LaRoque, V M Gehman, M F Kidd, and M Chen. An Improved Limit on Pauli-Exclusion-Principle Forbidden Atomic Transitions. *Foundations of Physics*, 42(8):1015–1030, 2012.
- [19] Corinaldesi and E. MODEL OF A DYNAMICAL THEORY OF THE PAULI PRINCIPLE. *Nuovo Cim.*, 43:937, 1967.
- [20] Abner Shimony. Proposed Experiment to Test the Possible Time Dependence of the Onset of the Pauli Exclusion Principle. *Quantum Information Processing*, 5(4):277–286, aug 2006.
- [21] F. Reines and H. W. Sobel. Test of the Pauli Exclusion Principle for Atomic

Electrons. *Physical Review Letters*, 32(17):954–954, apr 1974.

- [22] R. Bernabei, P. Belli, F. Cappella, R. Cerulli, C. J. Dai, A. D’Angelo, H. L. He, A. Incicchitti, H. H. Kuang, X. H. Ma, F. Montecchia, F. Nozzoli, D. Prosperi, X. D. Sheng, and Z. P. Ye. New search for processes violating the Pauli exclusion principle in sodium and in iodine. *The European Physical Journal C*, 62(2):327–332, jul 2009.
- [23] G. Bellini, S. Bonetti, M. Buizza Avanzini, B. Caccianiga, D. D’Angelo, D. Franco, M. Giammarchi, P. Lombardi, L. Ludhova, E. Meroni, L. Miramonti, L. Perasso, G. Ranucci, A. Re, Y. Suvorov, J. Benziger, L. Cadonati, A. Pocar, F. Calaprice, A. Chavarria, F. Dalnoki-Veress, C. Galbiati, A. Goretti, Andrea Ianni, M. Leung, B. Loer, R. Saldanha, J. Xu, C. Carraro, S. Davini, E. Guardincerri, G. Manuzio, M. Pallavicini, S. Perasso, P. Rissi, C. Salvo, G. Testera, S. Zavatarelli, H. De Kerret, D. Kryn, M. Obolensky, D. Vignaud, A. Derbin, V. Muratova, A. Etenko, E. Litvinovich, I. MacHulin, A. Sabelnikov, M. Skorokhvatov, S. Sukhotin, K. Fomenko, O. Smirnov, A. Sotnikov, O. Zaimidoroga, S. Gazzana, C. Ghiano, Aldo Ianni, G. Korga, D. Montanari, A. Razeto, R. Tartaglia, M. Goeger-Neff, T. Lewke, Q. Meindl, L. Oberauer, F. Von Feilitzsch, Y. Winter, M. Wurm, C. Grieb, S. Hardy, M. Joyce, S. Manecki, L. Papp, R. S. Raghavan, D. Rountree, R. B. Vogelaar, W. Maneschg, S. Schönert, H. Simgen, G. Zuzel, M. Misiaszek, M. Wojcik, F. Ortica, and A. Romani. New experimental limits on the Pauli-forbidden transitions in C12 nuclei obtained with 485 days Borexino data. *Physical Review C - Nuclear Physics*, 81(3):034317, mar 2010.
- [24] E Nolte, T Brunner, T Faestermann, A Gillitzer, G Korschinek, D Muller, B Schneck, D Weselka, V N Novikov, A A Pomansky, A Ljubicic, D Miljanic, and H Vonach. Accelerator mass spectrometry for tests of the Pauli exclusion principle and for detection of beta beta decay products. *Journal of Physics G: Nuclear and Particle Physics*, 17(S):S355, 1991.
- [25] D Javorsek, M Bourgeois, D Elmore, E Fischbach, D Hillegonds, J Marder, T Miller, H Rohrs, M Stohler, and S Vogt. New experimental test of the pauli exclusion principle using accelerator mass spectrometry. *Physical review letters*, 85(13):2701–4, 2000.
- [26] G. Hilscher. *Festkörperphysik 1*. 2009.
- [27] S Di Matteo and L Sperandio. VIP Technical Note IR - 4. Technical report, 2005.

- [28] J. V. Mallow, J. P. Desclaux, and A. J. Freeman. Dirac-Fock method for muonic atoms: Transition energies, wave functions, and charge densities. *Physical Review A*, 17(6):1804–1809, 1978.
- [29] C. Curceanu. EVALUATION OF THE X-RAY TRANSITION ENERGIES FOR THE PAULI-PRINCIPLE-VIOLATING ATOMIC TRANSITIONS IN SEVERAL ELEMENTS BY USING THE DIRAC-FOCK METHOD. 2013.
- [30] Emilio Gatti and Pavel Rehak. Semiconductor drift chamber - An application of a novel charge transport scheme. *Nuclear Instruments and Methods In Physics Research*, 225(3):608–614, sep 1984.
- [31] P Lechner and H Soltau. Silicon Drift Detectors for SIDDHARTA - Mounting, Bonding and Testing. Technical report.
- [32] M Cargnelli, M Bragadireanu, M Catitti, C Fiorini, T Frizzi, H Fuhrmann, F Ghio, B Girolami, C Guaraldo, M Iliescu, T Ishiwatari, K Itahashi, M Iwasaki, P Kienle, T Koike, P Lechner, P Levi Sandri, V Lucherini, A Longoni, J Marton, T Ponta, D L Sirghi, F Sirghi, H Soltau, L Struder, E Widmann, and J Zmeskal. Silicon drift detectors for hadronic atom research - SIDDHARTA. *Proceedings, International Conference on Exotic Atoms and Related Topics (EXA 2005)*, pages 1–8, 2005.
- [33] W. Leo. *Techniques for Nuclear and Particle Physics Experiments*. 2 edition, 1993.
- [34] Eljen Technology. <http://www.eljentechnology.com/>.
- [35] AdvanSiD. AdvanSiD ASD-SiPM3S-P. Technical report, 2012.
- [36] A. T.A.M. De Waele. Pulse-tube refrigerators: principle, recent developments, and prospects. *Physica B: Condensed Matter*, 280(1-4):479–482, 2000.
- [37] S. Agostinelli, J. Allison, K. Amako, J. Apostolakis, H. Araujo, P. Arce, M. Asai, D. Axen, S. Banerjee, G. Barrand, F. Behner, L. Bellagamba, J. Boudreau, L. Broglia, A. Brunengo, H. Burkhardt, S. Chauvie, J. Chuma, R. Chytracek, G. Cooperman, G. Cosmo, P. Degtyarenko, A. Dell'Acqua, G. Depaola, D. Dietrich, R. Enami, A. Feliciello, C. Ferguson, H. Fesefeldt, G. Folger, F. Foppiano, A. Forti, S. Garelli, S. Giani, R. Giannitrapani, D. Gibin, J. J. Gomez Cadenas, I. Gonzalez, G. Gracia Abril, G. Greeniaus, W. Greiner, V. Grichine, A. Grossheim, S. Guatelli, P. Gumplinger, R. Hamatsu, K. Hashimoto, H. Hasui, A. Heikkinen,

A. Howard, V. Ivanchenko, A. Johnson, F. W. Jones, J. Kallenbach, N. Kanaya, M. Kawabata, Y. Kawabata, M. Kawaguti, S. Kelner, P. Kent, A. Kimura, T. Kodama, R. Kokoulin, M. Kossov, H. Kurashige, E. Lamanna, T. Lampen, V. Lara, V. Lefebure, F. Lei, M. Liendl, W. Lockman, F. Longo, S. Magni, M. Maire, E. Medernach, K. Minamimoto, P. Mora de Freitas, Y. Morita, K. Murakami, M. Nagamatu, R. Nartallo, P. Nieminen, T. Nishimura, K. Ohtsubo, M. Okamura, S. O’Neale, Y. Oohata, K. Paech, J. Perl, A. Pfeiffer, M. G. Pia, F. Ranjard, A. Rybin, S. Sadilov, E. di Salvo, G. Santin, T. Sasaki, N. Savvas, Y. Sawada, S. Scherer, S. Sei, V. Sirotenko, D. Smith, N. Starkov, H. Stoecker, J. Sulkimo, M. Takahata, S. Tanaka, E. Tcherniaev, E. Safai Tehrani, M. Tropeano, P. Truscott, H. Uno, L. Urban, P. Urban, M. Verderi, A. Walkden, W. Wander, H. Weber, J. P. Wellisch, T. Wenaus, D. C. Williams, D. Wright, T. Yamada, H. Yoshida, and D. Zschiesche. GEANT4 - A simulation toolkit. *Nuclear Instruments and Methods in Physics Research, Section A: Accelerators, Spectrometers, Detectors and Associated Equipment*, 506(3):250–303, 2003.

- [38] T. K. Gaisser and T. Stanev. Cosmic Rays. *The European Physical Journal C*, 15(1-4):150–156, 2000.
- [39] M. Ambrosio, R. Antolini, A. Baldini, G. C. Barbarino, B. C. Barish, G. Battistoni, Y. Becherini, R. Bellotti, C. Bemporad, P. Bernardini, H. Bilokon, C. Bower, M. Brigida, S. Bussino, F. Cafagna, M. Calicchio, D. Campana, M. Carboni, R. Caruso, S. Cecchini, F. Cei, V. Chiarella, B. C. Choudhary, S. Coutu, M. Cozzi, G. de Cataldo, H. Dekhissi, C. de Marzo, I. de Mitri, J. Derkaoui, M. de Vincenzi, A. di Credico, O. Erriquez, C. Favuzzi, C. Forti, P. Fusco, G. Giacomelli, G. Giannini, N. Giglietto, M. Giorgini, M. Grassi, A. Grillo, F. Guarino, C. Gustavino, A. Habig, K. Hanson, R. Heinz, E. Iarocci, E. Katsavounidis, I. Katsavounidis, E. Kearns, H. Kim, S. Kyriazopoulou, E. Lamanna, C. Lane, D. S. Levin, P. Lipari, N. P. Longley, M. J. Longo, F. Loparco, G. Mancarella, G. Mandrioli, A. Margiotta, A. Marini, D. Martello, A. Marzari-Chiesa, M. N. Mazziotta, D. G. Michael, P. Monacelli, T. Montaruli, M. Monteno, S. Mufson, J. Musser, D. Nicolò, R. Nolty, C. Orth, G. Osteria, O. Palamara, V. Patera, L. Patrizii, R. Pazzi, C. W. Peck, L. Perrone, S. Petrera, P. Pistilli, V. Popa, A. Rainò, J. Reynoldson, F. Ronga, C. Satriano, E. Scapparone, K. Scholberg, A. Sciubba, P. Serra, M. Sioli, G. Sirri, M. Sitta, P. Spinelli, M. Spinetti, M. Spurio, R. Steinberg, J. L. Stone, L. R. Sulak, A. Surdo, G. Tarlè, M. Vakili, C. W. Walter, and R. Webb. Measurement of the residual energy of muons in the Gran Sasso underground laboratories. *Astroparticle Physics*, 19(3):313–328, 2003.

- [40] G. Bellini, J. Benziger, D. Bick, G. Bonfini, D. Bravo, M. Buizza Avanzini, B. Caccianiga, L. Cadonati, F. Calaprice, C. Carraro, P. Cavalcante, A. Chavarria, A. Chepurnov, D. D'Angelo, S. Davini, A. Derbin, A. Etenko, F. von Feilitzsch, K. Fomenko, D. Franco, C. Galbiati, S. Gazzana, C. Ghiano, M. Giannarchi, M. Goeger-Neff, A. Goretti, L. Grandi, E. Guardincerri, C. Hagner, S. Hardy, Aldo Ianni, Andrea Ianni, D. Korablev, G. Korga, Y. Koshio, D. Kryn, M. Laubenstein, T. Lewke, E. Litvinovich, B. Loer, F. Lombardi, P. Lombardi, L. Ludhova, I. Machulin, S. Manecki, W. Maneschg, G. Manuzio, Q. Meindl, E. Meroni, L. Miramonti, M. Misiaszek, D. Montanari, P. Mosteiro, V. Muratova, L. Oberauer, M. Obolensky, F. Ortica, K. Otis, M. Pallavicini, L. Papp, L. Perasso, S. Perasso, A. Pocar, R. S. Raghavan, G. Ranucci, A. Razeto, A. Re, A. Romani, A. Sabelnikov, R. Saldanha, C. Salvo, S. Schönert, H. Simgen, M. Skorokhvatov, O. Smirnov, A. Sotnikov, S. Sukhotin, Y. Suvorov, R. Tartaglia, G. Testera, D. Vignaud, R. B. Vogelaar, J. Winter, M. Wojcik, A. Wright, M. Wurm, J. Xu, O. Zaimidoroga, S. Zavatarelli, and G. Zuzel. Cosmic-muon flux and annual modulation in Borexino at 3800 m water-equivalent depth. *Journal of Cosmology and Astroparticle Physics*, 08:049, 2013.
- [41] M. Haffke, L. Baudis, T. Bruch, A. D. Ferella, T. Marrodán Undagoitia, M. Schumann, Y. F. Te, and A. Van Der Schaaf. Background measurements in the Gran Sasso Underground Laboratory. *Nuclear Instruments and Methods in Physics Research, Section A: Accelerators, Spectrometers, Detectors and Associated Equipment*, 643(1):36–41, 2011.
- [42] C. Bucci, S. Capelli, M. Carrettoni, M. Clemenza, O. Cremonesi, L. Gironi, P. Gorla, C. Maiano, A. Nucciotti, L. Pattavina, M. Pavan, M. Pedretti, S. Pirro, E. Previtali, and M. Sisti. Background study and Monte Carlo simulations for large-mass bolometers. *European Physical Journal A*, 41(2):155–168, 2009.
- [43] J. Marton and A. Pichler. Pauli Exclusion Principle test with electrons at LNGS - Continuation of FWF P25529-N20. Technical report, 2017.
- [44] J. L. Campbell, Leonard McDonald, Theodore Hopman, and Tibor Papp. Simulations of Si(Li) x-ray detector response. *X-Ray Spectrometry*, 30(4):230–241, 2001.
- [45] S. Okada. E570 analysis summary. Technical report.
- [46] M. Krause and Oliver J. Natural Widths of Atomic K and L Levels, K-alpha X-Ray Lines and Several KLL Auger Lines. *Journal of Physical and Chemical*

*Reference Data*, 8(2), 1979.



# Appendices



# A. Data Acquisition Layout

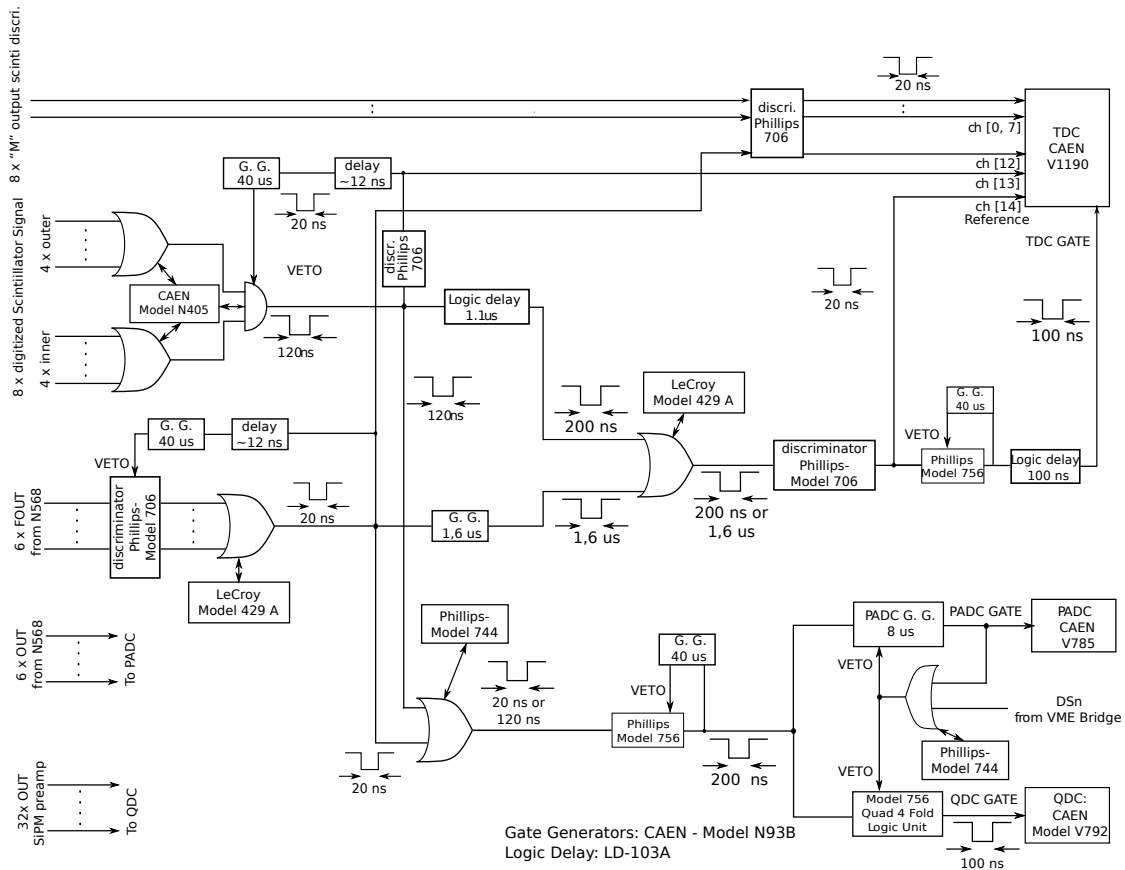


Figure A.1.: Layout of the data acquisition system for the VIP2 experiment